Bridging the Gap between Laboratory Lithium Ferro Phopshate Degradation and Field Operation

by

R. W. Kenyon

B.A., University of Vermont, 2013

A thesis submitted to the

Faculty of the Graduate School of the

University of Colorado in partial fulfillment

of the requirements for the degree of

Master of Science

Department of Electrical, Computer, and Energy Engineering

2017

This thesis entitled:
Bridging the Gap between Laboratory Lithium Ferro Phopshate Degradation and Field Operation
written by R. W. Kenyon
has been approved for the Department of Electrical, Computer, and Energy Engineering

_____

Prof. Alan Mickelson

_____

Prof. Frank Barnes

_____

Prof. Sean Shaheen

Date _____

The final copy of this thesis has been examined by the signatories, and we find that both the content and the form meet acceptable presentation standards of scholarly work in the above mentioned discipline.

Kenyon, R. W. (M.S. Electrical, Computer, and Energy Engineering)

Bridging the Gap between Laboratory Lithium Ferro Phopshate Degradation and Field Operation

Thesis directed by Prof. Alan Mickelson

Deterioration and capacity fade, i.e. ageing, of Lithium Ferro Phosphate(LFP) cells, a thermally stable Lithium chemistry with promise for Energy Storage System (ESS) applications, is typically protracted through laboratory measurements such as Electrochemical Impedance Spectroscopy or full charge and discharge cycles with accompanying Coulomb counting. When installed in remote microgrid stations such as intermediary sites of a communications system, these measurements are often not possible, which makes the identification and quantification of deterioration challenging for LFP batteries deployed in real world settings. Herein lies the impetus to identify and extract other metrics indicating ageing from the operational profiles of remote LFP installations.

The University of Colorado testbed is a Wifi Long Distance network funded by the IEEE Smart Villages group and located on the front range of Colorado. Each station is outfitted with an isolated microgrid consisting of LFP batteries and Solar PV panels, as well as a microcontroller system taking current, voltage, and temperature measurements at a five second resolution. After a collection period spanning 7 months (April - October, 2017), this data is analyzed and Schedule Points representing 100 % State of Charge are identified. The Coulombic and Battery Energy efficiency, that is, the ratio of charge delivered verse charge recovered and the ratio of energy delivered verse energy recovered, respectively, of each cycle is then derived and further analysis is performed to identify any ageing trends. While a quantiable amount of ageing and further statements about the State of Health are not possible without further analysis, a clear decline in efficiencies representing ageing is indentified, establishing a basis for further work to quantify these metrics.

Dedication

To Jessa and Frida, the ones who suffered most from my thesis engagement; the woods await us.

Acknowledgements

A special thanks to the Institute of Electrical and Electronics Engineers Smart Villages group which funded the University of Colorado Boulder Wireless Long Distance testbed. Without this support, the testbed and requisite power systems, upon which this work was performed, would not have been possible.

Thank you to Professor Alan Mickelson for the project, technical support, and for being reliably consistent source of thoughtful comments and instigating criticism.

To Professor Frank Barnes, thank you for being a presence to discuss any number of energy, and non-energy, related ideas throughout my Masters experience.

To the testbed team of 2016 and 2017, thank you all for your help in establishing and fabricating these stations on the front range of Colorado. The many different aspects and sheer volume of work necessary to develop an operating system was far more than a single graduate student could ever hope to accomplish in such a short time span.

Contents

Chapter

Tables

Table

Figures

Figure

Chapter 1

Introduction

In the last decade, renewable energy sources such as Wind and Solar have realized a price per unit energy drop to levels below the marginal cost of conventional fossil fuels[14, 12, 7, 10]. Within the United States there are many states pursuing Renewable Portfolio Standards (RPSs) that mandate a certain level of renewable generation; consider two of the largest states by population, California and New York, pursuing 50% Renewable Energy (RE) penetrations by 2030[24, 7]. Worldwide, the entirety of countries have agreed to the standards set with the Paris Climate Accord in which each country submits National Determined Contributions (NDCs) pledging to a certain level of domestic Renewable generation[24]. The benefits of RESs extends beyond the low cost and carbon emission reductions to decreased susceptibility to fuel price volatility as well as reducing energy imports (an energy security concern)[33]. Thus, there are many reasons for the increased penetration of RESs on the grid; but, the integration of said RESs is more challenging than simply bringing more Solar Photovoltaics and Wind Turbines online.

The rapid increase in RESs on the grid is creating a more abrasive application for conventional generators that mitigate the intrinsic variability in the demand profile[51]. The rapid ramping possible with Solar Photovoltaic (PV) generation (See Figure 1.1) on a cloudy day forces backup conventional generation through many rapid ramping cycles, which increases costs and carbon emissions through the inefficient use of the fossil fuel asset. With higher and higher levels of RESs on the grid, the conventional generator is evidently not the solution for RE variable output mitigation due to these inefficiencies. A potential panacea to the variable output of RES is the

Battery Energy Storage System(BESS).

From the standpoint of an ESS, electrochemical systems have the benefit of rapid response (quick ramping), scalability, and modularity[33, 46, 7, 11]. They've received ample technological funding; e.g. from 2009 - 2012, the US Department of Energy (DOE) invested over $10 billion in BESS technology[60], subsidization which is commonplace for most emerging energy technologies. The plummeting costs of Lithium batteries in even the past few years (80% reduction from 2011 - 2017[34, 8, 4]), has encouraged the installation of grid scale BESSs. Rapid growth rates are evident from the numbers; 221 MW of installed capacity at the end of 2015 and a projected 4 GW of installed capacity worldwide by 2020, a 1700% increase.

The Lithium Ferro Phosphate (LFP) battery is of the Lithium Ion family, but of a superior thermal stability than its Lithium relatives[31]. With an energy density of 110 Wh/kg, three times that of Lead Acid chemistries, the LFP cell is finding wide application in many scenarios such as Electric Vehicles[42], utility scale BESSs[6, 52], and microgrids both isolated and grid connected[1]. Due to the rapid emergence of Lithium batteries, and the expected lifetimes far exceeding 2,000 cycles to an 80% DOD, statistical data on Lithium battery decay for standard applications is not yet widely available. As a result, the majority of data on Lithium battery degradation/capacity fade, has origin in the laboratory, where highly regulated charge/discharge cycles occur in a controlled climate[16, 23, 40, 50]. While effective modelling techniques to derive degradation rates from state estimation have been borne out of these laboratory tests, they're often computationally intensive and less applicable to low capital installations[40]. As a result, there is valid concern for the expected life of Lithium batteries with application in non laboratory settings.

1.1 Why Laboratory Battery Testing Doesn't Map to Physical Systems

As previously mentioned, the bulk of testing of Lithium batteries in a laboratory setting is highly regulated and generally periodic throughout the experiment[13, 62]. Certainly, within a laboratory the isolation of variables is of upmost concern in order to derive results applicable to single causes; however, as a result, the practical application of BESSs is typically done with little

relation between degradation in the lab and anticipated degradation in the field. See Table 1.1 for a comparison of a variety of Lithium battery applications and associated levels of control as a representation of the mapping between real world application and laboratory results.

Table 1.1: The variety of Lithium battery applications and defining characteristics.

Application	**Climate Control**	**Charge Control**	**Discharge Control**
Electric Vehicles	Moderate	Complete	Moderate
Utility Scale	Complete	Complete	Complete
Utility Scale (Solar Coupled)	Complete	Moderate	Complete
Microgrid (Grid Coupled)	Moderate	Complete	Complete
Microgrid (Isolated)	Minimal	Minimal	Minimal

In the case of Electric Vehicles, the rate of charge is highly regulated due to the conformity of Electric Vehicle Service Equipment (EVSE) to charging standards[18]. Additionally, because of the mobility application and the zero tolerance for inoperation, the Lithium packs are climate controlled to maintain operable temperatures within extremes[42]. Utilty scale applications, particularly those that are not exclusively coupled to Solar PV charging, are operable with total control of climate, charge, and discharge characteristics[3]. In this way, the degradation of utility scale BESSs will likely be the closest fit to laboratory results. For the case of microgrids, particularly those that are isolated from a steady power source (i.e. the grid), control is minimal[1]. The BESS will charge when a Solar and/or wind resource is available, discharge when required, and generally because of the isolated installation, climate control isn't a concern due to a lack of available energy (the BESS itself would be required to power any climate control).

1.2 Challenges with Microgrid Installations

An additional aspect that serves to further separate the laboratory setting with actual implementation of BESSs in isolated microgrids, particularly Renewable Energy Source (RES) powered, is the variability in the RES output. Consider the variability of the Solar resource at one of the

CU Boulder testbed stations in June of 2017, depicted in 1.1. For the case of an isolated microgrid, where this RES is the only energy source available to charge the BESS, the rapid ramping due to the high variability causes a highly inconsistent rate of charge. The Lithium battery charging literature is lacking with respect to the analysis of these rapid fluctuations with regards to degradation rates.

Figure 1.1: Shown is the Solar Photovoltaic power output of the 100W panel located at the Wilderness Place station throughout the day of June 17. The total output was 321.7 Wh, which wasn't sufficient to reach a 100% SOC on this day (see Appendix Fig. A.1). Of note is the rapid ramping in output due to meteorological events in the form of cloud cover and afternoon thundershowers. In the case of a single ESS, this rapid ramping in PV output causes the inverse in ramping on the ESS, which serves to further displace actual operation of an ESS as compared to laboratory testing.

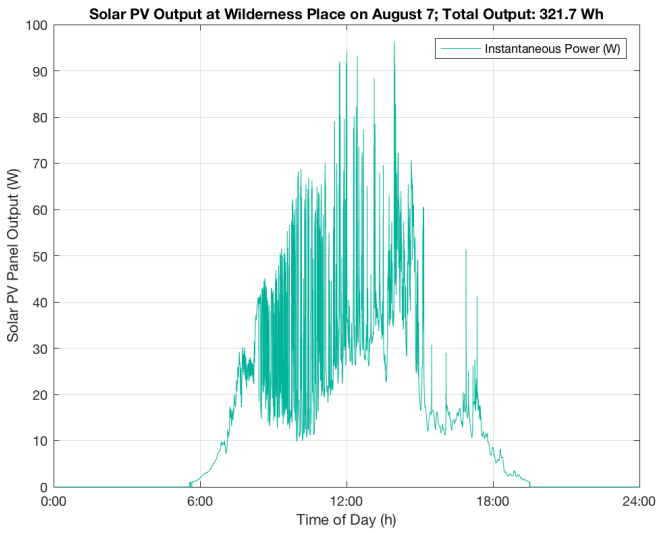

Additionally, as shown in Fig. 1.2 as compared to the output of the same station shown in Fig. 1.2, there are days when the RES production is very low. As a result, the BESS will experience a deeper discharge as it is forced to supply the energy called upon by the load. This results in varying Depth of Discharges (DODs) (see Fig. 5.19 for a show of variability at the Wilderness Place station), which is variability not often accounted for in laboratory settings. As a result of these inconsistencies with respect to the microgrid BESS, it is difficult to project degradation study results to life expectancies of Lithium batteries in said applications. It is therefore of interest to the

battery community as a whole to retain data of Lithium battery operation in a microgrid setting in order to tease out degradation and how it relates to the operational inconsistencies that the BESS will experience throughout its application. This is the focus of this work.

Figure 1.2: The output from the same system as from the data in Fig. 1.1 on August 7, a day of low insolation. While the variabiilty, as measured in magnitude of ramping, is evidently much less than on June 17, the overall output is significantly reduced at a total of 106 Wh. This low insolation day required the ESS to supply the balance of energy necessary to power the Load, as opposed to maintaining a higher SOC. This results in a much larger Depth of Discharge.

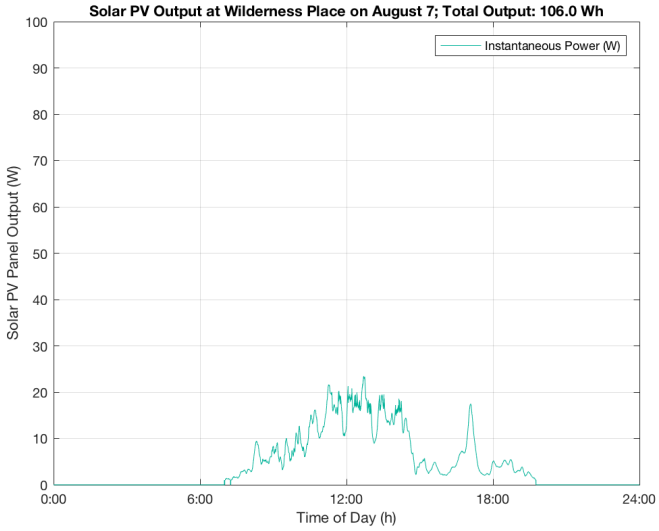

1.3 Statement of Thesis

A project at the University of Colorado Boulder under funding from the IEEE Smart Villages groupd required the installation of a variety of Lithium BESSs, along with Solar PV RESs as the singular source of energy for the BESSs, to act as an uninterruptible power supply for a communcations tested. The power systems are, by definition, isolated microgrids. These installations will have monitoring systems capable of tracking the current and voltage states of the BESS, as well as tracking the temperature of the system. With the inconsistencies in BESS operation in microgrid applications, the thesis can now be stated:

With uninterrupted data sets of the voltage, current, and temperature states of a Lithium Ferro Phosphate battery operating as the BESS of a microgrid, will the identification of complete cycles and subsequent derivation of the 'Coulombic Efficiency' and 'Battery Energy Efficiency' per cycle yield an identifiable degradation or capacity fade in the BESS? Additionally, if degradation/capacity fade is indentified through these metrics, can a quantitative statement be made about the current SOH?

Chapter 2

Lithium Ferro Phosphate Battery Technology

Compared to the Lead Acid battery, the primary (single use) cell introduced by Volta in 1800[60] and the secondary (rechargeable) invented by Gaston Plante in 1859[46], Lithium battery technology is a nascent electrochemical storage solution following an early 90's commercial introduction of the phosphate/oxide family by Sony in its Nexelion camcorder[9]. While the Lead and Sulfuric acid contained in the Lead Acid battery are environmentally noxious, the Lithium battery family yields a much safer alternative with no leaking acids or otherwise harmful emissions over its useful lifetime[46], a lifetime up to five times greater than leading Lead Acid technologies[5, 59]. Nickel-Cadmium, Zinc-Bromine, and Sodium-Sulfur chemistries are commercially available, but the Lithium family is eclipsing those as the leading storage technology[29]. Lithium, element number 3 in the periodic table, is extracted as a constituent of either Ore, Brine, or Clay, with Australia, Chile and Argentina the current primary source countries[53]. Its small atomic number and resulting small ionic radius make it particularly well suited for diffusion through the solid electrolyte[9]. In 2016, the primary consumer of Lithium Ion Batteries (LIBs) was the cellphone/laptop industry at approximately 75%[53] of marketshare.

The Lithium battery takes the same form as it's predecessors, with an anode (negative terminal) and cathode (positive terminal) separated by an electrolyte. The anode is typically a carbon material such as graphite, or perhaps in the near future, graphene[29]. The cathode is composed of either a Lithium metal oxide, or Lithium metal phosphate. More common cathode compounds are Lithium Cobalt Oxide (LCO), Lithium Manganese Oxide (LiMnO), and Lithium Ferro Phosphate

Figure 2.1: A representation of the cation (positively charged ion), anion (negatively charged ion), and electron movement through a Lithium cell. 'A' represents either the load, or the charging apparatus. In the case of charging, current flows from the cathode to the anode through the electrolyte. While discharging, the opposite. [9]. Image from [9].

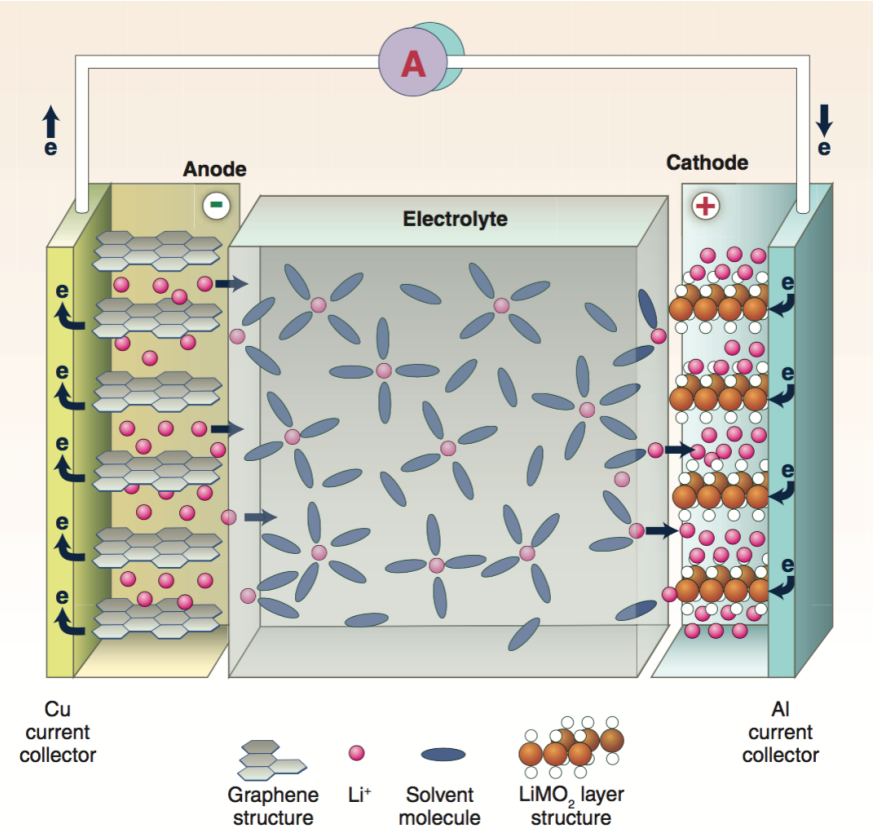

(LiFePO)[5]. With phosphates, as opposed to oxides, the oxygen bonds are much stronger which prevents the oxygen from being released through cycling, thus preventing the combustion issues most prevalent with the LCO chemistry[59]; consider the recent recall of the Samsung Galaxy. For this reason, in addition to the superior thermal stability[39], Lithium Ferro Phosphate has become a popular chemistry for large energy storage systems.

2.1 Half Cell Reactions

In the case of the Lithium Ferro Phosphate cells, we can use the image of Fig. 2.1 to understand the reduction/oxidation reactions which occur during charge and discharge. During discharge, when a load is placed in series across the terminals of the cell, the following half cell

reactions take place at the cathode and anode, where reduction occurs at the cathode, and reduction occurs at the anode:

$$\mathrm{FePO_4 + Li^+ + e^- \longrightarrow LiFePO_4} \tag{2.1}$$

$$\mathrm{LiC_6 \longrightarrow C_6 + Li^+ + e^-} \tag{2.2}$$

The full redox reaction during discharge of the LFP cell is then:

$$\mathrm{FePO_4 + LiC_6 \longrightarrow LiFePO_4 + C_6} \tag{2.3}$$

In the case of charging, because these are secondary, and therefore rechargeable, batteries, the reverse occurs when an overpotential is applied across the terminals. Oxidation at the cathode, reduction at the anode, and the following half cell reactions, cathode first:

$$\mathrm{LiFePO_4 \longrightarrow FePO_4 + Li^+ + e^-} \tag{2.4}$$

$$\mathrm{C_6 + Li^+ + e^- \longrightarrow LiC_6} \tag{2.5}$$

$$\mathrm{LiFePO_4 + C_6 \longrightarrow FePO_4 + LiC_6} \tag{2.6}$$

where the full redox reaction during charging is the final line of Equation 2.4.

2.2 Mechanisms of Degradation and Ageing in Lithium Batteries

The mechanisms causing degradation in Lithium Ferro Phosphate cells are numerous and varying across the anode, electrolyte, and cathode[57]. Due to the many contributing factors, the overall degradation of the cell is non-linear, and highly susceptible to variations in use, i.e. temperature adjusts and charge/discharge rate have been shown to have orders of magnitude effects on capacity fade[43]. While the scope of this work will focus primarily on tracking coulombic efficiency drift and battery energy efficiency decreases as a lump sum of internal degradation, a brief overview of the primary contributing factors is nonetheless offered.

(1) **Solid Electrode Interface (SEI) Growth:** Located between the Carbon based anode and the electrolyte, the SEI prevents these two battery components from reacting while

allowing the passage of Li-ions. Because the anode operates outside the range of electrochemical stability, particularly when the cell is charged and the anode is at a low potential, reduction of Li-ions and electrolyte occurs on the anode surface and the SEI grows in thickness[57]. With cycling, this layer continues to expand, resulting in increases of overall cell resistance, which results in heat losses during cycling; $P_{loss} = i^2 R_{cell}$[50, 28]. This growth and subsequent increase in cell resistance is a clear indicator of cell ageing, and will be searched for in the data as an increase in overall increases in charging energy.

(2) **Loss of Lithium:** The number of Lithium atoms available for redox reactions is reduced by multiple effects. The first condition occurs as reduction at the SEI, as Li-ions and the electrolyte form. Additionally, corrosion of C_6Li, causes a decrease in the quantitiy of Li atoms available for cycling. This reduction in Lithium atoms directly reduces the the number of possible reactions, resulting in a capacity decrease because the cations avaiable for transfer through the electrolyte to balance the transfer of electrons through the external circuit is reduced. [29, 60].

(3) **Mechanical Stress:** As cations and anions repeatedly intercalate within their respective lattice structure through redox reactions, expansion of the lattice structure occurs. This results in R_{cell} increases due to a reduction in conductive area[50, 9]. This will compound with the SEI growth as an overall R_{cell} increase which ought be evident within the data.

2.3 Calendar Ageing

In addition to degradation due to cycling, Lithium batteries are also susceptible to capacity fade when in storage. This phenomenon is the result side reactions occuring at the anode in which cyclable Lithium is reduced at the SEI[26, 61]. A portion of this reduction is typically reversible, which means the capacity loss is only a factor for the subsequent cycle after storage and is then recovered after a full charge[25]. Nonetheless, a certain loss of capacity due to the loss of cyclable Lithium to SEI growth occurs throughout the unused life of Lithium battery[16]. Experiments

dedicated to identifying and quantifying this calendrical ageing have found minimal decary for storage at 30 degrees C, to as much as 30% loss of capacity for storage at 60 degrees C in 450 days[16, 26, 25]. Calendar ageing is a factor that will have a far greater influence on Electric Vehicle Lithium battery pack degradation analysis because the large majority of time will be spent idle i.e. most vehicles are parked 95% of the time[18]. Calendar ageing occurs in tandem with cycle affected ageing, with the latter being the more dominant cause of degradation[25].

2.4 Lithium Battery Charging

The optimal charging protocol for Lithium batteries is the Constant Current Constant Voltage (CCCV) scheme, which optimizes the charging time and reduces the power loss througout the cycle[23, 50, 19]. The standard CCCV charging implementation consists of two steps, aptly named the Constant Current phase, followed by the Constant Voltage phase. During the CC portion of the charge, a 1C charge rate is forced across the pack while the voltage rise to N x 3.6V, where N is the number of cells in series[61]. In the case of a nominal 12.8V pack, the CC phase continues until a voltage of 14.4V is reached. Subsequently, the CV phase is implemented in which the cell(s) are held at a voltage of N x 3.6V until the charging current tapers to a rate of 0.02C. At this point, the cell(s) are considered be at a 100% State of Charge (SOC).

As is readily apparent, the CCCV charging protocol requires a continous power supply to manage the consistent 1C rate during the CC phase of the charge. In fact, the magnitude of energy transfer increases as the battery obtains a higher SOC due to the increased voltage verse the constant current transfer. As a result, it can be expected that optimal charging of Lithium batteries isn't possible with a Solar resource, because the embedded intermittencies and single daily peak power don't permit a CC phase of charging at all times. The bulk of literature focused on capacity fade implements the CCCV protocol during the charging portion of testing[1, 43, 26, 25, 61]. Due to the optimality of CCCV, it can therefore be expected that LFP batteries subject to the variability in Solar PV charging may exhibit shorter useful lifetimes than those subject exclusively to CCCV. This constitutes yet another aspect in which field testing results are expected to deviate from

laboratory testing.

2.5 State of Charge Assessment

Of primary interest during the operation of a battery pack is the State of Charge (SOC), which is a representation of the residual capacity of the pack[19]. This isn't to be confused with the State of Energy (SOE), which is represents the available energy of the pack and is more challenging to assess due to the non-linear relation between the SOC and voltage profile of the Lithium cell(See Fig. 2.2). A variety of methods can be implemented to perform SOC analysis, with varying degrees of accuracy based on multiple factors. A brief review of these methods is now presented.

Figure 2.2: The following shows the voltage across the Bioenno Power 12.8V, 200 Ah battery pack during a constant current discharge at 0.06C until cutoff at approximately 9.5V. This is not the open circuit voltage of the pack due to measurement occuring under load. The open circuit voltage will be higher at a given SOC, but still less than the voltage during charging. This battery is deployed at the SPSC station and is one of two subjects being analyzed for this work.

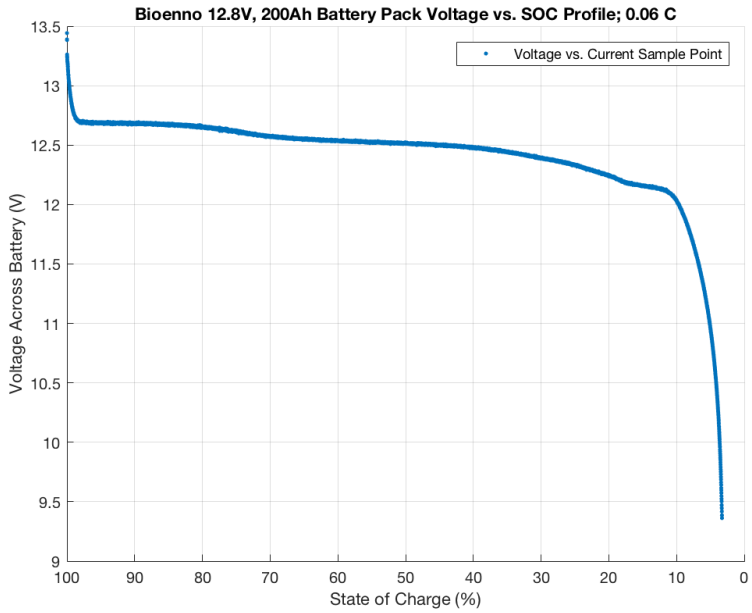

2.5.1 Open Circuit Voltage

The Open Circuit Voltage (OCV) is a function of the SOC, and as such the reverse mapping can result in a SOC estimation by simple voltage measurement[31]. Earlier chemistries, such as Lead Acid, portray a more linear relationship between the OCV and SOC[9], unlike the profile of Lithium technologies which exhibit a plateau as evident in Fig. 2.2. The result is a less than ideal accuracy with OCV/SOC estimation for Lithium battery technologies. Additionally, for the case of a remote microgrid powering a communications system, the data of which is only accessible when the system is functioning, the measurement of OCV becomes complicated requiring a secondary, and remotely switachable ESS. Finally, although a voltage vs. SOC curve is clearly still measurable while the pack is under load, the shape and voltage values is highly dependent on the rate of current flow[23]. A method such as Kalman filtering allows for the mapping of these varying voltage levels as a function of discharge rate to the OCV; however, the ageing of the cell will cause the efficacy of the mapping to diminish.

2.5.2 Electrochemical Impedance Spectroscopy(EIS)

Perhaps the most effective method at determing the SOC and State of Health(SOH) is Electrochemical Impedance Spectroscopy (EIS). The process of EIS is to apply a small varying frequency AC to the battery at a DC voltage matched to the battery voltage such that no net current flow occurs. Although batteries are highly non-linear, the small scale of the applied voltage corresponds to small portion of the I-V curve and a linear response matching an equivalent circuit can be expected. The response of the battery is captured by a frequency analyzer, after which the real and imaginary impedances are plotted against each other on a Nyquist plot. The resultant plots contain the footprints of a variety of R, and RC equivalent circuits. Various phenomena related to different SOCs such as the mass transfer resistance, double layer impedance, and diffusion resistance among others can then be derived from plots[35]. Additionally, due to the increase of diffusion resistance at lower SOCs and a mapping between the two, an accurate measurement of SOC can be derived from

EIS. This method is particularly well suited for tracking the development of internal phenomena related to the overall lifetime of a battery[1, 41] because of the sensitivity of the method.

Although EIS is an effective method for determining the SOC and SOH, it is challenging to implement in a remote station for a few reasons. First, the battery must be disconnected from any loads before EIS can be applied, which means a secondary ESS would need to be colocated at the station with a reliable switching mechanism, the design and implementation of which was not a part of the budget for the testbed upon which this work was performed. Second, a Frequency Response Analyzers (FRAs) is required, in addition to the Voltage Controlled Oscillator (VCO) and DC source, to perform the requisite analysis of induced currents. While the presence of a secondary ESS is not unfeasible with respect to this project, as there are ample subjects regarding the fail-safeing of an entire ESS through partitioning, the sensitive electronics are beyond the budget of the project upon which this research was performed. Additionally, while the supplanting of the FRA with the Arduino measurement system is a sound suggestion, we'll find in Section 3.4.2 that the 60 mA resolution of the current monitor is far too great for EIS, which requires micro-amp resolutions to capture milli Ohm impedances with a millivolt signal[63].

2.5.3 Coulomb Counting

Relatively inexpensive to implement, Coulomb counting is the process in which the current flow out of, or into, the battery is tracked and then integrated with respect to time to arrive at an ampere-hour value of delivered, or recovered, charge, respectively. This is then compared to the known capacity of the battery pack, the quotient of which provides the SOC, or the case of discharge:

$$SOC(t) = \frac{Q_{full} - Q_{delivered}(t)}{Q_{full}} \times 100\% \tag{2.7}$$

where Q_{full} is the capacity of the battery and $Q_{delivered}$ is the integration of discharge current with respect to time. Equation 2.7 doesn't include corrective factors necessary for SOC calculation during charging.

Due to the electrochemical nature of the battery in which a predetermined number of reactions

can result, a determination of the number of coulombs delivered since the start of a cycle allows an accurate determination of the SOC[59, 19]. Typically, the quantity of Coulombs counted during discharge factors directly to the total capacity and yields a one to one mapping of the SOC. In the case of charging, an inefficiency of Coulomb counting arises due to side reactions within the cells, and thus a greater number of Coulombs, as compared to the number discharged, are required to fully charge a cell[50, 35]. The ratio between the number of delivered, to recovered, Coulombs is known as the 'Coulombic Efficiency'. The process of Coulomb counting is the primary method used in this work for deriving the SOC and identifying ageing.

2.5.4 Kalman Filtering

With well developed parameters for the model of a battery cell, a method called Kalman Filtering can be employed for improving SOC estimation when suitable computational power is available. The process involves the comprehensive measurement of voltage verse SOC curves are varying rates of discharge and charge, which are then used to correct Coulomb counting derivations of the SOC[35]. Additional complexity and a corresponding reduction in protracted error is achieved by a second level of filtering to account for hysteresis effects[35]. Hysteresis causings over and under voltages across the cell after charge and discharge cycles, respectively, which remain until after a thorough relaxation period[48]. Kalman filtering provides a method to reduce uncertainty in the Coulomb counting method of SOC determination by correcting the SOC result with a set of predetermined votage vs. SOC parameters. As such, it requires a robust development of a battery state profile before deployment that can be used for this corrective approach[19]. However, these internal parameters vary as the cells age, and thus the Kalman filtering process requires consistent updating to maintain its accuracy throughout the life of a battery pack. Within this work, a separate data analysis method is used to identify 100% SOC points, the remaining SOC accuracy considered secondary to this identification. Thus, because the accuracy of the Kalman filtering process hinges on the accuracy of the internal parameters, the lifetime variance of which is the topic of this work, it was not attempted in this project.

2.6 Identifying Ageing in a Remote Battery Station

The two primary methods for identifying ageing in a Lithium cell are to perform periodic full charge/discharge cycles of the cell to redefine the actual capacity of the cell, or to use EIS and identify variance in the equivalent circuit which can be related to internal phenonmenon. The focus of this is work is identify Lithium Ferro Phosphate ageing with neither of those methods, when the battery is seldom accessible, and removing the battery from the system results in a total system shutdown and is thus considered unacceptable. Certainly, this will greatly effect the ability to accurately identify ageing, but the situation is more reflective of an actual LFP installation. Investigation into the ageing mechanisms has yielded an understanding of what conditions may be indentified in a continous data set of state variables and how they contribute to overall battery degradation.

2.6.1 Coulombic Efficiency

Capacity fade, or the reduction in charge availability for redox reductions, is most effectively identfied through periodic full discharge/charge actions on the cell. Clearly, this isn't possible in a remote setting in which the battery must continuously provide energy for operation. Furthermore, over the lifetime of a battery, it isn't an economical action to periodically cycle a battery when the length of lifetime is a concern, as this simply serves to reduce the lifetime. What is measurable with respect to capacity at a remote station is the total charge delivered, and the total charge recovered, between 100% State of Charge points throughout the operation of the battery. 'Coulombic Efficiency' is defined as the quotient of the total charge delivered, and the total charge recoverd, as shown in Equation 2.8.

$$\eta_{CE} = \frac{Q_{delivered}}{Q_{recovered}} \tag{2.8}$$

where η_{CE} represents this efficiency, $Q_{delivered}$ is the total charge delivered, and $Q_{recovered}$ is the total charge recovered. η is typically quite high, and values exceeding 99% are expected for Lithium technologies. The discrepancy in charge delivered vs. charge recovered is due to

the occurrence of side reactions within the cell, such as the reduction of Lithium resulting in SEI growth, during the charging process[41]. Because current measurements occur outside of the battery pack, side reactions that occur during discharge are not captured within $Q_{delivered}$. However, the acceptance of $Q_{delivered}$ as the datum to which $Q_{recovered}$ ought to approach, the Coulombic efficiency provides a valuable insight into operational efficiency of the battery.

Figure 2.3: Shown are the impacts of total charge and total discharge fluctuations. The x-axis is interpreted as the value of the variable with respect to the other, which is being held constant. The y-axis is the resultant efficiency. Because the total discharge is in the numerator, the impact on Coulombic efficiency is linear with respect to fluctuations due to error. The total discharge, residing in the denominator, has a non linear effect on the Coulombic efficiency, but is approximately linear for slight variations.

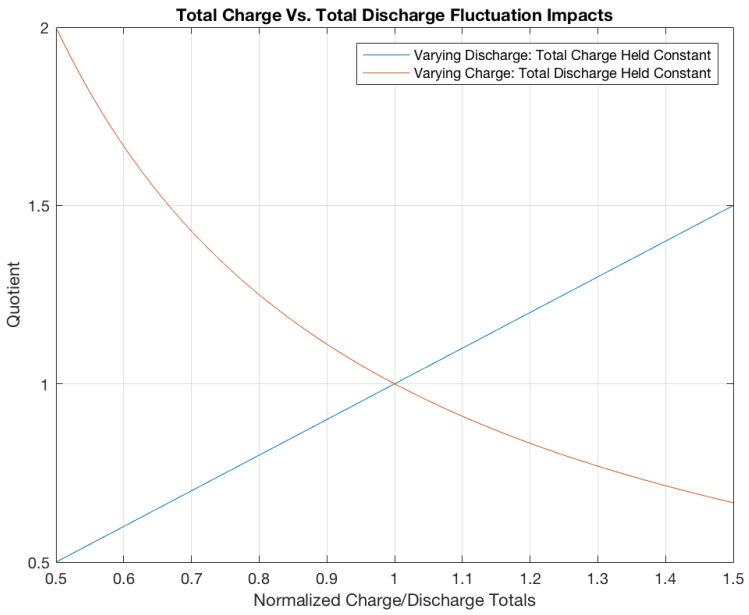

By tracking the current flow through a battery pack and integrating this with respect to time, the total charge delivered, and charge recovered, can be effectively measured. In an uninterupted data set, the challenge comes in determining the start and stop points of this charge tracking. In this work, 'Schedule Points (SP)', i.e. operational points at which a 100% SOC is reasonably identified, are identified and used to mark cycle start/stop points. This identification process is discussed in Section 4.1. Of potential concern upon identifying these SPs is the influence of error

on η_{CE}.

Figure 2.3 shows the influence of fluctuating either the total charge, or total discharge, during a cycle while holding the other constant. Because the total discharge is in the numerator, there is a linear relationship between fluctuations and resulting efficiency. Total charge fluctuations have non-linear effects on the efficiency due to the inverse relationship. While this complicates the calculation of η_{CE} in a system with non-trivial error, we'll soon find in the analysis that the total charge time throughout a cycle is a fraction of the total discharge time, which serves to reduce the total charge error and bring the error within a linear regime, i.e for values near parity, the inverse relation of total charge can be approximated as having a linear relation.

2.6.2 Battery Energy Efficiency

A second, Coulombic related type of efficiency comes in the form of the Battery Energy Efficiency (BEE). As the Coulombic efficiency is derived by intergrating the current over time during the charge/discharge portions of a cycle, the BEE is expounding by integrating the current/voltage product over the same time duration. In this way, the Coulombic efficiency is embedded in the BEE and as a result, the BEE is maximally bound by the Coulombic efficiency. The BEE is lower for other reasons such as the over potential necessary during charging, which necessitates a larger voltage across the cell during charge, as opposed to discharge voltages which are necessarily lower. The BEE is defined in a similar manner to the Coulombic efficiency, as shown in Equation 2.9

$$\Delta_E = \frac{E_D}{E_R} \tag{2.9}$$

Where E_D is the total energy delivered, and E_R is the total energy recovered. In addition to the over potential necessary to catalyze the redox reactions necessary for charging, there are additional factors causing voltage drops within the battery such internal resistances due to charge transfer and electrode conduction inefficiencies. Consider the rudimentary equivalent circuit for a Lithium cell shown in Fig. 2.4. While a more accurate equivalent circuit for a battery will contain more components in the form of RC pairs and additional parallel branches, the entirety

of this work from an analysis perspective takes place in the Direct Current (DC) domain and all frequency dependent components, the majority of which are modelled as capacitors that are open circuits at DC, can be effectively combined into a single internal resistance. As a result, the internal operations causing lower efficiencies can be effectively modelled as a single resistor in series with a voltage source. Note; all measurements occur at the V_{cell} terminals.

Figure 2.4: The Cell Equivalent Circuit model used in this work to represent internal resistance and the growth therein representing cell degradation. While internal capacitances are present, the only measureable quantities in this work are DC, at which frequency all capacitances are open circuits and the sum of all internal resistances can be represented by a single resistor. R_{int} is the representing resistance in this case.

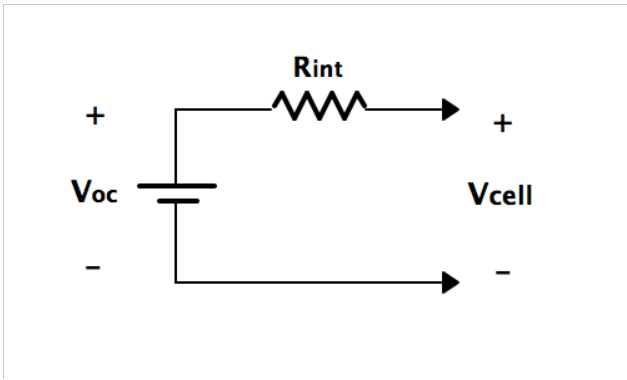

The energy delivered during discharge from t_0 to t_{tran}, where $tran$ represents a change from discharge to charge, is calculated as follows:

$$E_D = \int_{t_0}^{t_{tran}} i_D(t) \cdot v_{cell,D}(t) dt \tag{2.10}$$

For the case of charging, the energy recovered can be expressed as:

$$E_R = \int_{t_{tran}}^{t} (i_C(t) \cdot v_{oc,C}(t) + (i_C(t))^2 R_{int}) dt \tag{2.11}$$

Although the internal parameters are not directly measurable, e.g. V_{DC}, the presence of the i^2R losses indicate that an increase in R_{int} will result in an increase in the amount of recovered energy necessary for a full charge. As the internal resistance increases due to SEI growth, a decrease in accessible anode/cathode surface area available for intercalation, and corrosion of the copper current collector[26, 57, 47], a decrease in energy efficiency is expected because a larger voltage

drop will exist across the internal resistance, resulting in greater energy loss. This quantity should be readily apparent in continued monitoring of a battery system because full cycles are evident in the data and the calculation of power flow is the simple product of voltage and current, with energy flow the resultant summation over the discretized cycle. The identification of a decrease in Δ_E over cycling can therefore be accepted as a direct result of internal degradation.

2.6.3 Voltage Verse Depth of Discharge

Although the voltage verse depth of discharge profile displays substantial platueau between approximately 10% and 90%, it is expected throughout the lifetime of an LFP cell for the voltage values to drift with respect to a fresh cell and set depth of discharge levels[35, 57]. Fig. 2.5 shows the resultant voltage verse DOD curves for a new, and aged LFP cell, the results and chart of which are taken from source[35]. These curves are generated by Coulomb counting through very steady, and slow, rates of charge and discharge while tracking the voltage. While the exact relation of deviation to lifetime isn't know, a trend in the deviation over the lifetime of the batteries in this work will be sought.

Figure 2.5: A plot of the open circuit voltages and charge/discharge voltages of a fresh, and aged, LFP cell. Of interest is the spread in voltage measured with age. The image is from [35]

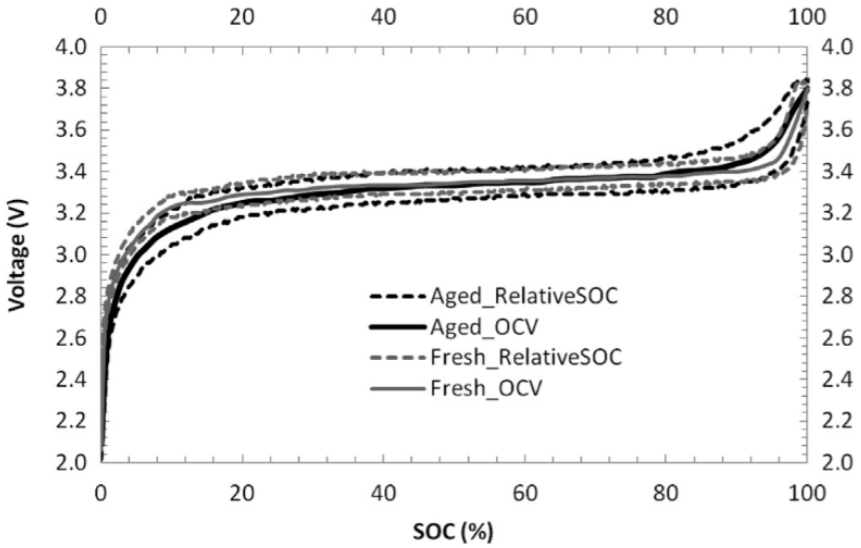

Although the charging rates of the LFP batteries in this work will vary, the rate of discharge and depth of discharge, particularly over the night, will be both consistent, and apprieciable. As such, by generating the voltage verse DOD curves of the battery for substantial cycles, deviations in this voltage can be mapped.

2.7 Battery Management Systems

One challenge with Lithium cells is their susceptibility to damage with even slight deviations from the operating voltage or temperature[31]; as a result, robust Battery Management Systems (BMSs) are required for Lithium battery packs. Each Lithium cell (or set of paralleled cells) requires a cell module mounted in parallel to monitor voltage, bypass charging current, and track the temperature of its assigned cell. When constructed as a pack, in which many cells are placed in series, a Battery Control Unit (BCU), will monitor the operation of each cell module such that it can isolate the pack in the event of an issue such as over temperature, over charge, or over discharge[29]. Although LIBs require a nontrivial amount of power elecronics for safe operation, the additional costs are outweighed by the benefits.

The nature of this work involves monitoring the current flow into, and out of, assembled LFP battery packs which internally house the BMS components. Therefore, consideration of the consumption of this management equipment is necessary to understand its effect on the Coulombic and Battery Energy efficiencies. The two cases, of charging and discharging, can be modeled as shown in Figures 2.6 and 2.7. Throughout the lifetime of the battery, no deviation in power consumption by the BMS is expected, per the manufacturer.

During discharge, the LFP pack will source an unmeasureable quantity of current, to the BMS, which can be expressed as:

$$i_{cm} = i_{lfp} - i_{bms} \tag{2.12}$$

For the case of charging, as shown in Fig. 2.7, we have the following relation:

$$i_{cm} = i_{lfp} + i_{bms} \tag{2.13}$$

Figure 2.6: The case of current flow within the a LFP battery with internal BMS circuitry during discharge.

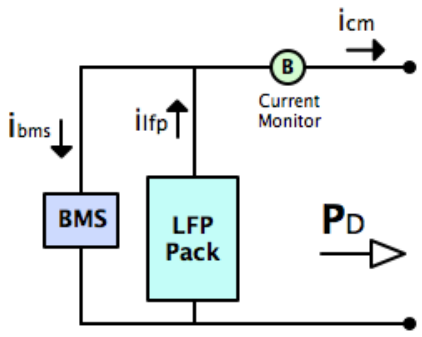

Figure 2.7: The case of current flow within a LFP battery with internal BMS circuitry during charge.

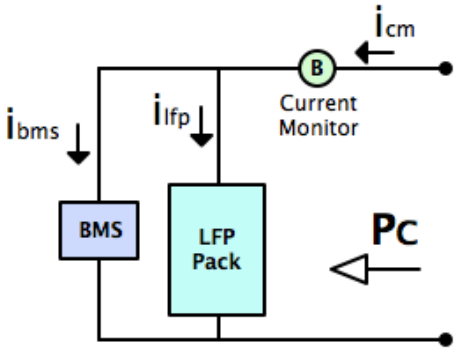

As evident from Equations 2.12 and 2.13, the presence of the internal BMS circuitry serves to cause an underestimate in the amount of current delivered by the LFP cells during discharging, and an over-estimate of the current consumed during charging. Even though the discrepancy is related to the time of each phase, charge or discharge, the only possible result is a decrease in Coulombic efficiency. However, the battery supply company was consulted for estimating the BMS consumption and a steady current consumption of $50\mu A$ was quoted, meaning an entire day of operation will only result in 1.2mAh of LFP consumption error. As will later be discussed, the current monitor error is found to be $\pm$ 30 mA for the battery measurements, which means the BMS consumption can be neglected as an influence based on the accuracy obtainable in this work.

Chapter 3

The System

In the Fall of 2016, the Institute of Electrical and Electronics Engineers (IEEE) Smart Village division providing funding to the University of Colorado at Boulder (CU Boulder) to commission a Wifi Long Distance (WiLD) testbed for the purpose of qualifying and troubleshooting a variety of wireless solutions applicable to non-connected regions of the world. Throughout the Spring of 2017, the testbed infrastructure was assembled and deployed by a team consisting of multiple iterations of undergraduate students lead by the author, and guided by Professor Alan Mickelson. Multiple papers have been written on the development, deployment, and results of the testbed experiment, including the following [27, 38, 37].

The testbed, as it exists today, consists of a base station located in the CU Boulder Engineering Center tower, three local stations found on the following CU Boulder properties (Wilderness Place, Space Sciences, South Complex), and a long distance site on Niwot ridge in the mountains to the west. As a result of the intentions of the testbed, i.e. to assess communications equipment over time, each station is equipped with a complete microgrid capable of managing all power needs with multiple days of battery backup in the event of a poor solar resource. The singular source of energy at each microgrid comes from a single Solar Photovoltaic (PV) panel, or in the case of the Niwot Ridge installation, an array of Solar PV panels.

The installation of the testbed to its current level of operation was a long and arduous process, involving a high level of commitment to many facets from site permissions, engineering designs, budget work, fabrication, and much more. Following the initial green light on the project, the

Figure 3.1: The layout of the entire local WiLD network, with a 5km radius circle superimposed on the map of Boulder, CO to provide a sense of distance from the Engineering Center Tower. The two stations housing the batteries under scrutiny for this work are 'Wilderness Place' and 'East Campus (a.k.a SPSC). Not shown is the Niwot Ride station, approximately 24 km to the west near the continental divide. This station's Energy Storage System isn't studied in this work.

Fall 2016 Semester was spent identifying suitable locations for the local and long range stations, preparing in-depth plans and schematics for approval from the Univeristy of Colorado Real Estate, Facilities Management, Office of Information Technology and the Dean's Office, and procuring approval for installation at each site. Following acquisition of the project funding late in 2016, the first half of the Spring 2017 Semester was spent sourcing the requisite equipment and fabricating the station electronics. With full approval for implementation, the local stations were installed late in the the Spring 2017 Semester. Because the main purpose of the power systems is to operate the radio equipment, the monitoring system wasn't fully operational at the same time as the radio systems which were considered priority. As a result, the monitoring systems and usable data acquisition came online in early June 2017, for both the Wilderness Place and SPSC stations, with partial data sets from Wilderness Place starting in April of 2017. See Fig. 3.1 for the layout of the local stations, where Wilderness Place and SPSC are found to the northweast of the Engineering Center Tower.

3.1 Station Components

The stations themselves are essentially embedded systems with a modest variety of power equipment, monitoring equipment, network devices, and a computational system. Power equipment consists of a Solar PV Max Power Point Tracking (MPPT) charge/load controller, a 12V voltage regulator, and a 5V buck converter. The distribution system is a simple fused bus, with a common ground rail. Three Direct Current (DC) Power over Ethernet (PoE) injectors provide power and and connectivity to the variety of radios that will eventually populate the system. At the time of this analysis, only one PoE injector was in use for a piece of LigoWave WiLD equipment. A network switch acts as a Local Area Network (LAN) bus between the WiLD radios and the Raspberry Pi 3. The Raspberry Pi 3 manages data storage and acts as a remotely accessible device at each station. Through the radio connection, the Pi at any testbed station can be accessed through SSH protocol. An Arduino microcontroller captures data every five seconds through a variety of voltage dividers, current monitors, and a temperature sensor, all of which is stored locally on the Pi and transmitted daily to the Server located in the Engineering Center Tower.

Figure 3.2: The layout of all the system components, mounted to a sheet of garolite with an assortment of stand-offs, bolts, and lock nuts. From upper left, clockwise: 20A MPPT Charge Controller, Negative Bus, Postive Fused Bus, 3 Power over Ethernet (PoE) Injectors, Raspberry Pi 3, Five Port Network Switch, 5V Buck Converter, 12V Voltage Regulator, Arduino, Voltage Dividers, Current Monitors. All items to the right of the Arduino and Charge Controller are lumped into the block 'Aggregate Load' in Fig. 3.3.

Because the system consists almost entirely of constant consumption devices, the Load consumption of the entire system is steady, nonwithstanding any equipment swaps. The WiLD radios do varying in power consumption at higher transmit powers, but these variations are slight with respect to the system consumption as a whole. Incidentally, this consistent consumption allows for a steady decrease in the State of Charge (SOC) following a day of good solar resource in which the ESS will achieve a 100% SOC and then decrease consistently through the night. This is a somewhat periodic occurence in the data and allows for the comparison of varying voltage verse SOC curves to tease out variance due to capacity fade.

Figure 3.3: Shown is a high level schematic of the Wilderness Place power system, with all consuming devices lumped into an aggregate load. The three current branches managed by the charge controller are individually monitored with ACS714 Hall Effect monitors. The voltages are also monitored, with the load and battery sharing a negative connection relative to the Arduino; hence, the negative voltage branch from the PV connection being the only negative reading necessary. See Figs. 3.8 and 3.9 for a break out of the voltage dividers.The primary differences between the Wilderness Place and SPSC stations are a 140W Solar PV panel and 200Ah battery at SPSC.

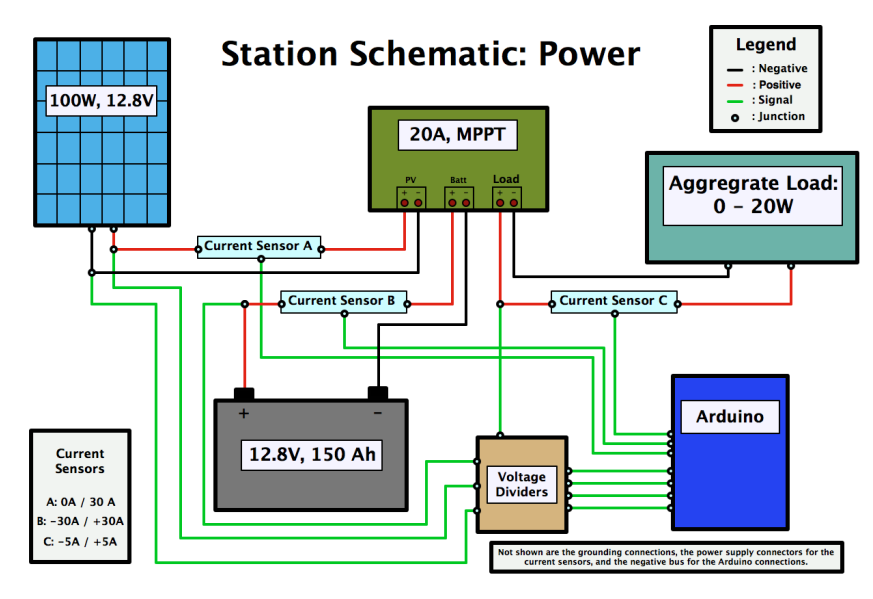

3.2 Bioenno Power

Bioenno Power, a subsidiary of *Bioenno Tech, LLC*, is a southern California company focused on the distribution of Lithium Ferro Phosphate (LFP) batteries and associated components. The

batteries under scrutiny for this work were sourced through Bioenno Power for the purpose of filling out the power systems for two of the testbed local client stations stations. Chosen were the LFP 12.8V, 150 Ah packs. Additionally, LFP compatible charge controllers were procured through Bioenno Power. Although the batteries were received as a turn-key installation with minimal knowledge of the internal setup, the company has been quite helpful by providing information regarding the internal components, such as the Battery Management System (BMS) and balancing cell modules, as well as data on charge/discharge characteristics corroborating the voltage vs. SOC profile of Fig. 2.2. Although two 12.8V, 150 Ah packs were ordered for the Wilderness Place and SPSC stations, for reasons unknown to the author, Bioenno Power supplied a 150 Ah and an upgraded 200 Ah battery, citing the upgrade as a 'thank you' for continued business. This doesn't affect the experiement, except to reduce the relative Depth of Discharge of the 200 Ah pack as compared to the 150 Ah pack.

3.2.1 Batteries

The Lithium Ferro Phosphate batteries supplied by Bioenno Power come as a complete device with all requisite onboard circuitry for safe operation installed and calibrated. The pack arrives in a waterproof container, with only negative and positive terminals exposed (See Fig. 3.4). Although the lack of immediate transparency in the battery system may be seen as an ostensible hindrance to the experiment, this was instead interpreted as another aspect of the system relating this experiment to actual implementation of ESS as opposed to laboratory testing. The 12.8V pack is intended for operation as the only ESS device in a system because multiple packs would have to communicate system state information, which isn't possible with the turnkey status of the Bioenno device. Regardless, the stations operate at a nominal 12 volts, and only required a single battery pack at the 150 Ah, 200 Ah capacities.

To better understand the internal circuitry of the battery packs, Bioenno Power was queried and subsequently provided key information. The cell around which the battery pack is designed is a cylindrical LFP 3.2V, 3300 mAh, of the 26650 variety. Thisnumerical style tag breaks as follows:

Figure 3.4: The 12.8V, 150 Ah battery pack supplied by Bioenno Power, which was eventually located at the Wilderness Place testbed station.

the first two digits represent the diameter, in mm; the remaining three digits are the length, also in mm. Therefore, these cyclindrical cells have a 26mm diameter, and are 650 mm length. In the case of the 150 Ah pack, the cell layout is 4S46P, i.e. 46 in parallel, and each 46P connected in series with three other sets of 46 in parallel. The 200 Ah pack is in a 4S61P configuration. As discussed in Section 2, Lithium batteries require Battery Management Systems (BMS) and balancing cell modules. The Bioenno packs contain these components, integrated and calibrated, for immediate deployment. As determined in section 2.7, the consumption of the BMS can be neglected with minimal impact beyond the resolution of the monitoring system.

3.2.2 Charge Controllers

The charge controllers located at the Wilderness Place and SPSC stations are both produced by Bioenno Power and are specfically designed for LFP chemistries. They are 20A Max Power Point Tracking (MPPT), with internal Load and Battery disconnect mechanisms. MPPT is a high efficiency method in which the controller tracks the variations in the power curve of the Solar module due to irradiance fluctuations and places the panel voltage at the MPP such that

the corresponding current output yields the maximum power output. In addition to managing the charging of the LFP battery through the MPPT of the solar module output, the controller also manages the Load/Battery connection such that the LFP isn't over discharged. As both the charge controller and the onboard BMS of the battery both provide overcharge and overdischarge protection, there is protection redundancy.

The controllers are flagged as being LFP specific; however, this is due to the protection mechanisms alone as the variations in solar output make the charge controller incapable of performing the optimal CCCV charging protocol for LFP chemistries. Regardless, the controller still performs a three stage charging protocol when possible, which consists of the following steps:

- **Bulk:** The maximum current flow possible is harnessed from the solar resource during charging when the SOC is betweeen 20 - 80%. This is comparable to the Constant Current (CC) phase through current magnitude comparisons; however, a constant current output isn't always possible due to irradiance.

- **Absorption:** For the remaining 80 - 100% of the charge cycle, the voltage is held constant while the current tapers off due to increasing cell voltages. This is akin to the Constant Voltage (CV) phase, and is quite comparable as the voltage is easily maintained through a variety of solar irradiances, even though the current may fluctuate widely.

- **Float:** Upon full charge, the charge controller matches the peak voltage of the battery pack and allows a trickle charge to flow to the pack after slight decreases in capacity due to load consumption balancing. This phase is beyond the CCCV charging protocol and is a factor of solar charging which increase utilization of the resource as available.

To better understand the operation of the Charge Controller when no solar resource is present,(i.e. the controller is only managing the exchange of power between the battery and load), this operation was simulated in the laboratory with a DC power source. Measurements of current flow into, and out of, the charge controller were taken with Fluke multimeters, as well as the voltage on the battery terminals and the load terminals. The voltage of the DC power source was adjusted

between the operating regime minimum and maximum while the load was maintained as a static resistance affecting an expected field consumption.

Table 3.1: The results of a laboratory test of the Bioenno Charge Controller used at the stations. This emulates the transfer of energy between the battery and load while no solar resource is present.

$\mathbf{V}_{Battery}(\mathbf{V})$	$\mathbf{V}_{Difference}(\mathbf{V})$	$\mathbf{I}_{Difference}(\mathbf{A})$	$\mathbf{P}_{Controller}(\mathbf{W})$
11.50	-0.02	0.005	0.03
12.15	0.02	0.005	0.09
12.85	0.03	0.005	0.11
14.10	0.02	0.005	0.11
14.90	0.03	0.005	0.13
15.70	0.03	0.005	0.15

As is evident from the results, higher voltages cause an increase in consumption through a non-linear relation by the charge controller, which serves to lower the efficiency. However, what is of interest for the purposes of this experiment is the steady difference in current. This result will allow a more rigorous Coulomb counting analysis in preceding sections.

3.2.3 Solar Photovoltaic Panels

The Renewable Energy Sources (RESs) are simple polycrystalline solar cell panels rated at 140W for the SPSC station, and 100W for the Wilderness station. The discrepancy in output power is due to a higher load demand at the SPSC station in the form of a second Raspberry Pi and WiLD radio to simulate additional clients on the load. $V_{oc} = 22.3V$ under Nominal Operating Cell Temperature (NOCT) conditions, which placed a lower bound on the negative voltage divider shown in Fig. 3.9 at apporximately -12V. An I_{sc} of 8.48A keeps the panel output well below 50% of the charge controller capabilities, a factor that likely reduces the efficiency the charge controller itself. The panels are ballast mounted to the roof at each station. While this method is ideal from an implementation standpoint (no roof penetrations), it reduces efficiency because the maximum angle possible is only 20° from horizontal, while the ideal fixed tilt angle on the front range is 33.5°.

3.3 The Stations

The following provides a brief overview of the two stations of the CU Boulder WiLD testbed which house the two batteries under scrutiny for this work.

3.3.1 Wilderness Place

The Wilderness Place station was actually commissioned ahead of the rest of the testbed with a separate set of funding. At the end of the Summer of 2016 the station was installed and powered with an LFP battery pack that was assembled by the author. This pack isn't part of this analysis for multiple reasons, the least of which is an inconsistent data set due to an undersized pack for the load leading to repeated load disconnects and partial data sets. The 150 Ah LFP pack was initially installed in a separate location with a larger solar panel in early April of 2017. Following upgrades to the system, the 150 Ah LFP pack was then deployed to the Wilderness Place station in early June of 2017. Interestingly, the larger panel caused different behavior between the charge controller and the battery protection system, leading to a different type of cycling. This is discussed in detail in Section 4.2. Since June of 2017, the Wilderness Place station has been operational with full current, voltage, and temperature monitoring. The station is shown in Fig. 3.5.

The metal structure to the right of the black container is an asethetic structure implemented on the entire Wilderness Place building to block the rooftop equipment. Incidentally, this also qualifies as an equipment ground and was utilized as such for the system. Additionally, this structure blocks the majority of the illumination of the Sun on the power system throughout the day which helps to reduce the midday temperature at this station.

3.3.2 Space Sciences (SPSC)

The Space Sciences installation, colloquially known as the SPSC, was commissioned at the end of May, 2017. Being the third station installed of the testbed, the power system bugs had

Figure 3.5: The Wilderness Place Station on the roof of the CU Boulder Wilderness Place building. The 100W panel is shown with the power feeds and grounding wire leading to the power system housed in the black container. The ballast system for the Solar panel is evident, as is the low angle which will significantly reduce output in the Winter, well beyond the reduction expected for a panel at an optimal angle. The WiLD radio can be seen on the top of the mast above the black system container.

all been eradicated and the system operated as intended from the first initialization. Thus, the data set for the SPSC station begins at the start of June. A second Raspberry Pi 3 and WiLD radio are colocated at the SPSC station to add a greater load on the communications system. The result of this colocation is an increased draw on the power system, which affects a greater Depth of Discharge (DOD).

As shown in Fig. 3.6, the grounding point for the SPSC station is the 45° angle brace attached to the concrete wall to the left of the black system container. The photo is of late afternoon when the system container is in the shade due to the wall located due west. Throughout the morning and mid-afternoon, the entire system is exposed to the Sun and very high temperatures are experienced within the container.

Figure 3.6: The Space Sciences (SPSC) system, located on the roof of the SPSC building on the CU Boulder campus. In the foreground is the 140W panel with the ballast mount system resulting in an approximate 15° angle from horizontal. The black container with the power system is visible beyond the panel, and the WiLD devices shown on the mast above the black container.

3.4 Data Capture

The microcontroller selected to measure and log the voltage, current, and temperature states of the two systems was the Arudino ATmega 2560. This device has 16 analog pins with a voltage swing of 0-5V and 1024 (2^{10}) bit resolution. A sketch (code) is uploaded to the device, after which the Arduino broadcasts the results of all measurements at a set periodicity of five seconds. These measurements are captured by a Raspberry Pi through a USB A/B cable, which logs the data by concatenating the reading with a .txt file created for the current day. The data set is truncated in real time at midnight, and a new file is created for the following day.

Issues with data capture have persisted throughout the duration of this experiment in that occasionally the microcontroller will seize operation. This is mitigated though an I/O connection

with the Pi which re-uploads the sketch to re-initiate data capture. Regardless, there exist periods of inconsistent data capture in the data set. Because the majority of the anaysis requires a complete set between Schedule Points, the truncation of the set with the close of each day allows for ease in identification of incomplete daily sets and the subsequent removal of these sets prior to analysis. A summary of the complete data sets is found in Section 4.

The nature of the analog measurements requires the microcontroller to assign a value representing an effectively continuous (the resolution of current theoretically goes to the charge of an electron, which is effectively continuous when compared to a 1024 bit controller) variable to either of the adjacent analog values. See Fig. 3.7 for a graphical respresentation. While the error of this system is based on the voltage dividers/current monitors and the associated 1024 bit resolution over the 0-5V analog pin range (see Sections 3.4.1 & 3.4.2 for the associated errors), variability in the measurements is reduced by sampling the analog output 1000 times over the five second interval, and then printing the average value over this interval; see Equation 3.1.

Figure 3.7: A depiction of discrete measurements of a continuous variable. In this diagram δ represents the measurement resolution, which varies for different voltage and current measurements and is described in Sections 3.4.1 & 3.4.2. The line represents the continuous current or voltage variables, while the flanking tickmarks are two adjacent analog measurement points. The microcontroller is restricted to assigning either of the flanking measurement points to a continuous variable that resides between them.

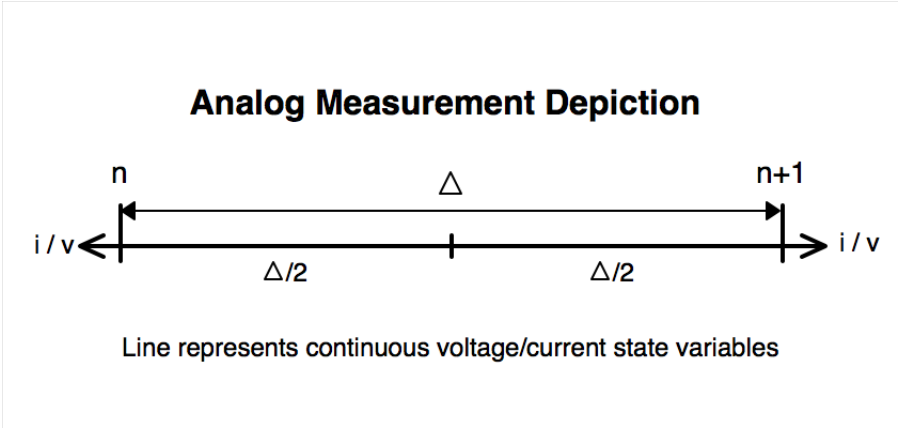

$$A(n) = \frac{\sum_{n=1}^{N} a(n)}{N} \tag{3.1}$$

where $A(n)$ represents the value printed by the Arduino, $a(n)$ represents one of the samples taken during the five second interval, and N is the number of samples. This method doesn't improve the accuracy, which is an aspect of calibration and is covered subsequently, but it does improve precision in that a minor fluctuation at the sample time that could trip an analog value which doesn't corroborate with the average value of the state variable through the five second interval isn't printed, but instead the average is taken.

3.4.1 Voltage Resolution

We can see from Fig. 3.7 that the error associated with any analog measurement is:

$$e(n) = \pm\frac{\Delta}{2} \tag{3.2}$$

where $e(n)$ is the sampling error, and Δ is the resolution of the analog device and the associated measurement device. This mathematical relation exists because a value beyond $\Delta/2$ of the analog point will trip an adjacent analog value. The base resolution of the Arduino microcontroller voltage capabilities, in which a voltage between 0 and 5V is monitored, is simply:

$$\Delta = \frac{5V - 0V}{1023} = 4.9mV \tag{3.3}$$

where n is the sample point between 0 and 1023 representing 0 - 5 volts.

Figure 3.8: The following voltage divider scheme is used to measure the postive voltages of the Solar PV panel, the LFP battery, and the Load. Although necessary to measure the higher votlages, this also causes an increase in the associated analog error of the measurement.

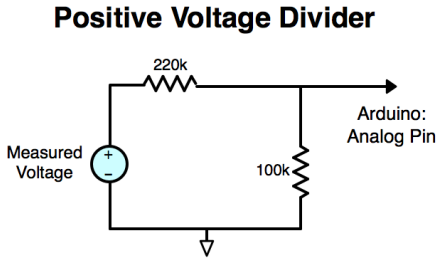

The system under continuous monitoring exhibits voltages from -8V to 15V. The voltages across the Load and LFP battery are confined to values between 9 - 15V, share a common ground,

and are positively tied. Monitoring of these voltages with an Arduino requires a voltage divider to restrict the analog sampling to a value between 0 and 5V. See Fig. 3.8. The scaling factor of this voltage divider yields a measurable voltage with respect to the Arduino, but the resultant resolution is:

$$\Delta_{PositiveVoltage} = (4.9mV)\frac{220k + 100k}{100k} = 15.7mV \tag{3.4}$$

A challenge arises in measuring the voltage across the Solar PV panel, which performs Max Power Point Tracking by adjusting the negative terminal at the charge controller farther negative with respect to the ground of the Load. To perform accurate measurements of this negative voltage relative to the ground of the load, summed voltage dividers were required with the Arduino 5V rail voltage as a constant voltage source. The schematic is shown in Fig. 3.9 and the associated resolution is $\Delta_{NegativeVoltage} = 19.1mV$.

Figure 3.9: Shown is the negative voltage divider implemented to monitor the negative voltage terminal of the Solar PV panel, which becomes negative with respect to the Load ground during MPPT operation.

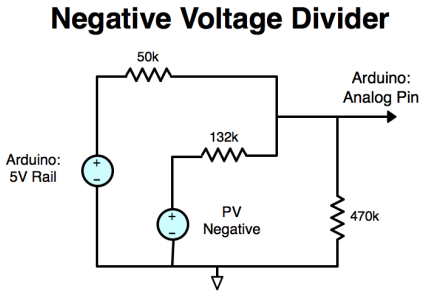

3.4.2 Current Resolution

The current monitors used in the system are of the Allegro ACS714 variety, which is a low power, low resistance current measurement solution that operates off of the Arduino rail voltage supply. The ACS714 makes use of the Hall effect, in which charge carriers exposed to a magentic field experience a trasverse deflection, thereby causing a voltage difference normal to the conductor, to measure current. This voltage is measured and scaled internally to fit the Arduino analog voltage

constraints, namely 0 to 5V. The device consists of a small PCB with Vcc, Vout, and Gnd connections which interface with the rail voltage, analog pin, and ground, of the Arduino, respectively. The device has a nominal 1.5% error at a standard temperature of 25°C. This error fluctuates over the operation regime, but over the anticipated temperatures at the system installation site (-15° - 50°C), the fluctuations are minimal and the error is taken as 1.5%.

Three separate current monitors are used for the three current carrying connections shown in Fig. 3.3. The PV current is tracked with a monitor capable of measuring 0A to 30A of positive current flow. The battery connection is monitored with a -30A to 30A capable device, and the Load is tracked with a -5A to 5A device. Each current monitor was selected to have the minimal measuring capacity overshoot to reduce the resolution and provide a more accurate measurement. The resolution of each device is simply:

$$\Delta = \frac{|Max_{measurement} - Min_{measurement}|}{1023} \tag{3.5}$$

The resultant resolution of the Battery current monitor is then:

$$\Delta_{Battery} = \frac{30A - (-30A)}{1023} = 58.6mA \tag{3.6}$$

A summary of the various measurement schemes and associated resolutions, for both the voltage dividers and the current monitors, is presented in Table 3.2.

Table 3.2: A summary of the various devices, measurement capabilities, and associated analog resolution constraints.

Device	**Position**	**Measurement Capabilities**	**Resolution**
Positive Voltage	Battery/Load/PV	0 to 16V	16 mV
Negative Voltage	PV	-13V to 6V	19 mV
Current Monitor	PV	0A to 30A	29 mA
Current Monitor	Battery	-30A to 30A	59 mA
Current Monitor	Load	-5A to 5A	10 mA

3.4.3 Initial Calibration

Due to the linear nature of the devices, the calibration was construed a simple task in which a variety of voltages, or currents, depending on the device being tested, were placed across the device while the Arduino tracked the resultant analog value. The analog outputs, as well as the applied voltage or current, were tracked and a mapping between the two was created. From this mapping, a linear relation was derived such that the analog values recorded by the Arduino would map to the physical quantity being measured. Although this initial calibration seemed sufficient, it was later found during analysis that the results were a bit unusual, leading to the conclusion and enactment of on-site calibrations at the Wilderness and SPSC stations, which is the topic of Section 3.4.4.

3.4.4 Calibration Refinement

Due to preliminary analysis yielding slightly nebulous results, an in-place calibration of the three current monitors at each station was deemed necessary to rectify the existing data and ensure the capture of more accurate measurements in the future. The calibration involved the setup of a power supply at the installation sites of the two Bioenno battery packs to create a controlled, variable current flow through the monitors, along with the testing equipment necessary to capture the current. The data capture portion of the calibration involved incrementally changing the current flow through the test circuit and noting the multimeter test value. Upon equilibrium in the Arduino measurement, which isn't immediate due to the five seconds between printing of the five second running average, this value was paired with the multimeter value.

To rectify existing data, a mapping between the existing values representing current flow and the actual values was created as follows. First, the difference between these two samples was defined as follows:

$$D(n) := M(n) - A(n) \tag{3.7}$$

where $M(n)$ represents the multimeter value at incremental current n, and $A(n)$ represents the same

Figure 3.10: The setup for the onsite calibration of the station current monitors. Note the power supply and power resistor providing a variable current flow for measurement purposes.

for the Arduino value. Upon calculation of $D(n)$ with the data sets of $M(n)$ and $A(n)$, a scatter plot of $D(n)$ vs. $A(n)$ was generated and linear regression used to determine the characteristics of the relationship. Linear regression is used due to the linear nature of the current monitors, as discussed in Section **??**. The results provide values for m and b for Equation 3.8.

$$D(n) = m[A(n)] + b \tag{3.8}$$

The corrected values are those of $M(n)$, so the goal is to map the $A(n)$ values to $M(n)$. The result is the following:

$$\begin{aligned} M(n) &= A(n) + D(n) \\ &= A(n) + m[A(n)] + b \\ &= A(n)[1 + m] + b \end{aligned} \tag{3.9}$$

With the derived values through linear regression of m and b for each of the three current monitors at the two stations, Wilderness Place and SPSC, the historic data can now be mapped to the the correct value using only the existing values. See Fig. A.2 in the Appendix for a graphical display of the applied correction.

Figure 3.11: The results of post data capture analysis of the battery current monitor at the SPSC installation. The linear regression fit will be used with Equation 3.9 to rectify existing data by mapping the previously recorded values to the correct values.

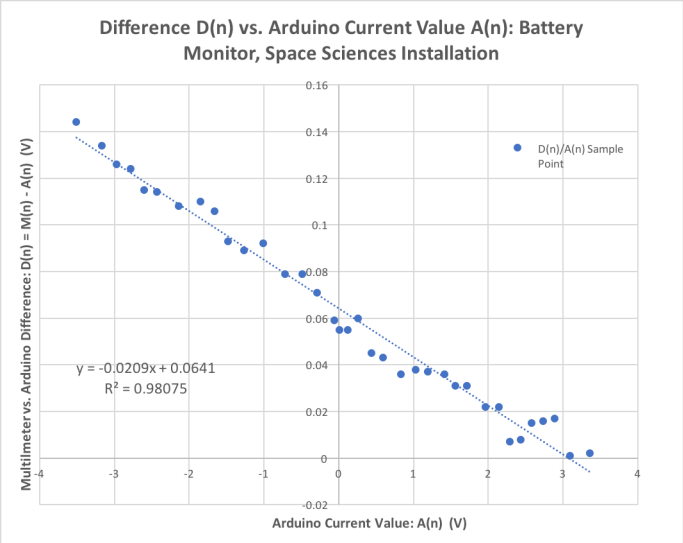

Table 3.3: A summary of the linear regression results following the onsite calibration of the Wilderness Place and SPSC installations.

Station	**Monitor**	**m**	**b**	R^2
Wilderness Place	Battery	-0.0184	-0.1584	0.949
Wilderness Place	Load	-0.0261	0.1648	0.975
Wilderness Place	Solar PV	-0.0291	0.0151	0.968
SPSC	Battery	-0.0209	0.0641	0.980
SPSC	Load	-0.0258	0.0685	0.988
SPSC	Solar PV	0.0066	0.0096	0.834

Chapter 4

Data

The data collected from the stations comes in the form of a .txt file which contains all lines of output from the Arduino with a five second temporal resolution for each day. The system is set up such that the data capture to each .txt is terminated at the end of each day and another file is created for the following day. In this way, the data from each day of operation is well categorized. The system is calibrated such that in the event of any restarts, upon a full start up data capture commences once again. An unavoidable consequence of system down time is an incomplete data set for a complete battery cycle, i.e. there will be missing data points while the battery is still undergoing state changes due to recovery charging from the charge controller, or continued load consumption during microcontroller hiccups. As a result, these system shutdown events result in the termination of a 'data string', which is defined here as a complete set of data with data points every five seconds. As a first step to data analysis, these data strings are identified and compiled before Schedule Points are identified.

As a brief example of the type of data collected throughout the experiment, Fig. 4.1 shows the compilation of all of the data collected througout the month of August at the Wilderness Place station.

4.1 Identifying Schedule Points

The foundation of this analysis relies on the ability to identify complete cycles of the battery pack through analysis of voltage and current behavior. Because of the charge controller and onboard

Figure 4.1: The resultant data capture of all 8 monitoring devices located at the Wilderness Place station. The upper four graphs are all voltage capture, the next three current capture, and the final temperature. Each line represents the discrete time series of captured data for a single day

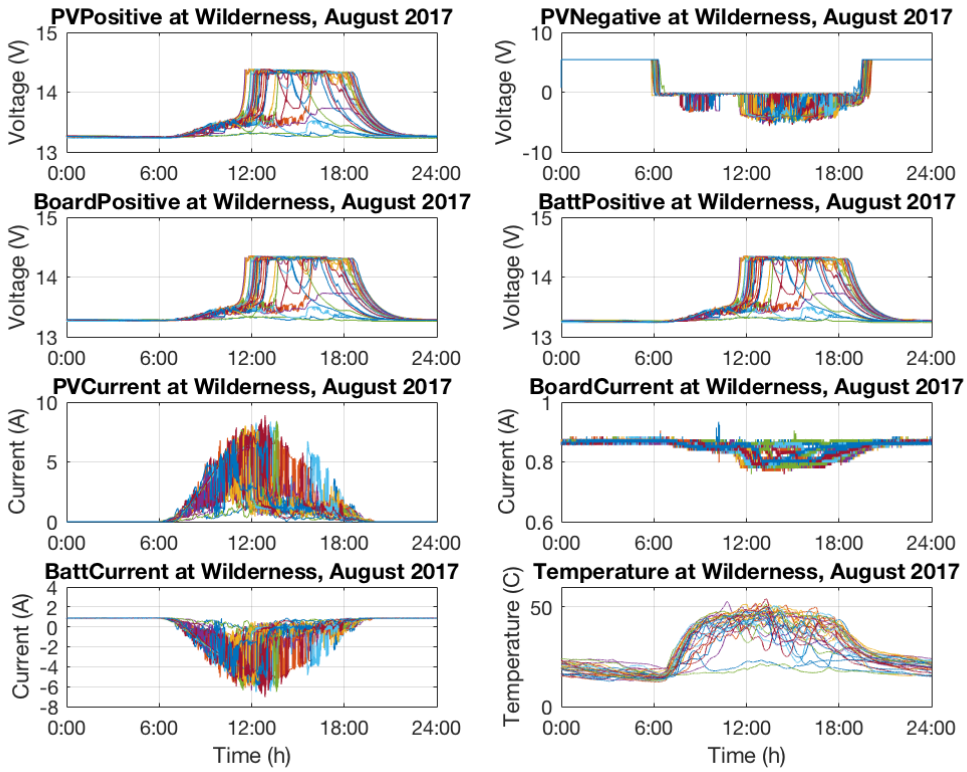

battery circuitry, combined with the oversized output of the solar resource as compared to an average night of load consumption, a 100% SOC state is anticipated to be achieved nearly everyday when the Solar resource is appreciable. In fact, it is found in the early data of the Wilderness Place set and the SPSC set that many small complete cycles occur throughout a day with good solar resource. These points of 100% SOC are known as 'Schedule Points' (SP), and with the data set, it is possible to identify all of these points through simultaneous analysis of the voltage and current flow at the battery interface. Upon identifying these points, the calculation of the SOC throughout each cycle is a simple summation.

The data is combed with moving windows to identifying the following criteria, which are accepted as necessary and sufficient for determining a SP:

- **Cutoff Voltage:** Voltage state variable must be a local maximum and correspond, within a set error, with a predetermined cutoff voltage imposed either by the LFP charge controller or the Battery BMS itself. This voltage must also represent an over voltage point, as a local maximum alone isn't sufficient for identifying an SP as local maximums always exist in the a data set, even on days with a low solar resource.

- **Current Cutoff:** The current flow must exhibit rapid ramping to an expected current flow corresponding with anticipated behavior at C_{full}. In the case of the Wilderness station, the Battery BMS terminates current flow and the Solar PV output is diverted to the load exclusively. With the SPSC station, the Solar PV is curtailed upon realization of a Schedule Point, and the battery begins supplying all power necessary to operate the load.

After preliminary analysis of the data, in which any incomplete portions are removed from the set and 'Strings' are determined by consistent data acquisition, the code shown in Algorithm 1 is implemented to identify the Schedule Points.

```
procedure SCHEDULE POINT IDENTIFICATION(String)
input:
    dataset(n,(v,i)) ← full string of uninterupted data, with voltage and current
    stringlen ← length of string
    overvoltage ← accepted cutoff voltage - 0.1V
    current tolerance ← accepted zero current
    off ← local bounds
output:
    sp(n,i,v) ← schedule point(position, current, voltage)
initialize:
    SP = []
    count = n + off
    if i > −stringlen then return false
    localmax = 0
    search = 1
for: n = start + off : stringlen - off
    if dataset(n,i) < current tolerance & search == 1 then
        local max = max(dataset(n − off : n + off, v))
        if local max > overvoltage then
            SP = [SP; countdataset(n, (i, v))]
            search = 0
            count = count + 1
```

The results of Algorithm 1 return the locations of Schedule Points within full strings of data. While the *for* loop implementation is of computational order N, and would otherwise take an enormous amount of time given the sets of data containing well over 1 million lines, the actual implementation incorporates logical arrays with MATLAB to rapidly identify the SPs. These SPs are then used as markers of a 100% SOC of the battery, with which complete charge/discharge (not necessarily a full discharge) are identified and statistics can be developed.

4.2 Wilderness Place Data

Shown in Fig. 4.2 is the data set for the string of April 4 - 11, during which time the battery was located at a separate station, not yet the Wilderness Place station. The overlaid red circles on both the upper (voltage) and lower (current) represent the SPs determined by the Algorithm discussed in Section 4.1. Obvious from the current chart is a rapid decrease in current flow into the battery, here represented as negative current flow. These instances, when corroborated with a peak voltage event, are the two separate voltage/current scenarios that together identify a SP.

As previously noted, the Wilderness Place battery was located at another site during the first two months of operation, during which time it was colocated with a 140W Solar PV panel. Upon relocation to the Wilderness Place station, a 100W Solar PV panel become the RES, which is the only change in equipment that occurred. This slight change seems to have affected the way the charge controller and BMS operate in cahoots to manage the over charge protection. Consider Fig. 4.2. Upon achieving a 100% SOC, the current flow from the battery immediately becomes positive and equal to the load consumption, which indicates the battery has become the power source for the load while the solar resource has been disconnected by the charge controller. The voltage of the battery is then observed to fall rapidly, until the charge controller brings the solar resource back online. This results in many cycles throughout the day.

Now consider the visualization of the string of data for July 8 through the 11th. During this time, the Wilderness Place battery was located at its intended station at the Wilderness Place station, with the smaller Solar PV panel at a rated output of 100W. Now, it can be seen that upon

Figure 4.2: The operation of the Wilderness Place battery system during April 4 - 11, 2017. Note the overlaid 100% SOC, represented as red circles.

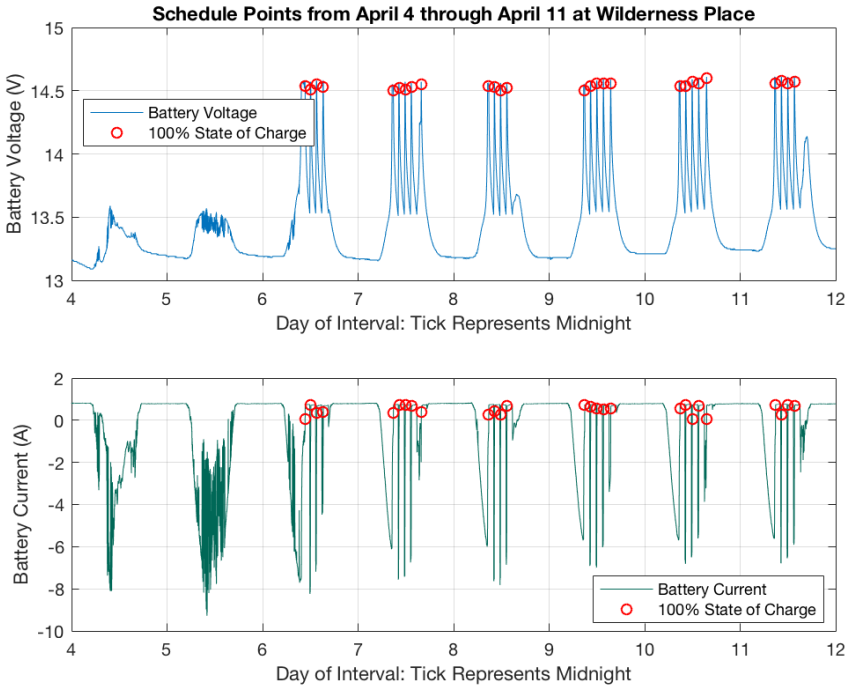

reaching a 100% SOC, the current flow from the battery drops to zero, which indicates that the battery BMS has disconnected the battery pack while the solar resource at the charge controller supplies power to the load. The fluctuations in current flow from zero are evidence of the battery pack supplying the balance in necessary power as the solar resource fluctuates. The result is far fewer cycles of the battery througout the day. We'll see throughout the analysis of the data that beyond the simple reduction in the quantity of cycles, this also causes some fluctuations in the Wilderness Place efficiency.

Table 4.1 provides a summary of each complete data set derived from the Wilderness Place raw data, as well as the number of Schedule Points identified with the SP Algorithm. Note the far greater number of Schedule Points during the month of April and May, as opposed to the number in the preceding months. This is due to the re-location of the battery pack to another site where the new Solar PV panel was 40W less in power output. As highlighted in Figures 4.2 and 4.2, the

Figure 4.3: The voltage and current profiles of the Wilderness Place battery from July 8 - 11. Overlaid are the determined Schedule Points representing 100% SOC, as determined by the Schedule Point algorithm.

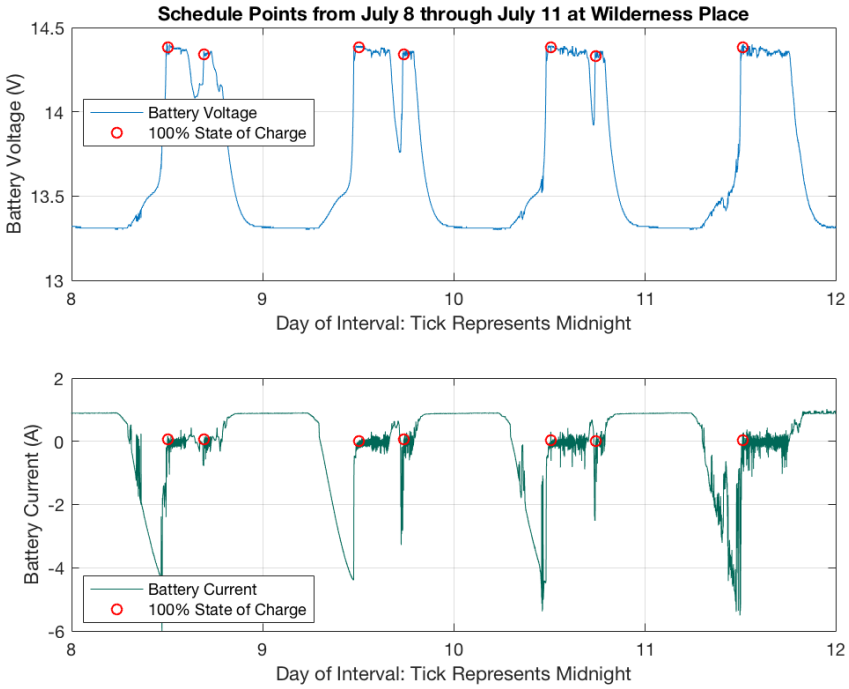

Table 4.1: A summary of the data set from the Wilderness Place station, including the parsed out complete strings and the quantity of identified Schedule Points within each String.

Month	**Days**	**Length(Days)**	**Total Schedule Points**
April	4 - 11	8	27
April	18 - 29	12	37
May	1 - 16	16	51
June	6 - 30	25	29
July	1 - 5	5	6
July	8 - 11	4	7
July	15 - 31	17	17
August	3 - 31	29	35
September	1 - 5	5	5
September	14 - 30	17	4
October	1 - 10	10	0
October	14 - 31	18	0

master control of the BMS/charge controller hiearchy was swapped with this relocation.

4.3 SPSC Data

The Space Sciences data exhibits the sort of cycles experienced by the Wilderness Place battery before being relocated with a smaller Solar PV panel. Fig. 4.4 shows the operational curves of the battery located at the SPSC station from July 1 to July 5. It is clear from these curves that the battery recovers charge until the voltage reaches a cutoff threshold around 14.7V, at which time the charge controller curtails all available Solar PV resource and sources the energy necessary to operate the load from the battery alone.

Figure 4.4: The battery voltage and current profiles at the Space Sciences station from July 1st to the 5th, with overlaid 100% SOC points. Note the similar operation to the Wilderness Place operation before relocation.

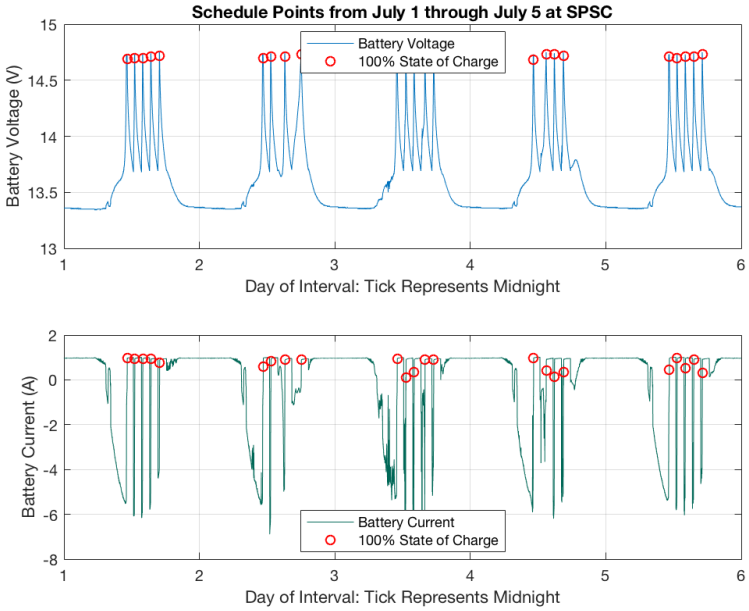

It should be noted that between the two operational procedures seen at the two stations, i.e. battery cutoff vs. solar cutoff, there is an obvious inefficiency in the operation which curtails the Solar entirely. Not only does this neglect the usage of the available Solar resource, which reduces the overall output of the Solar PV and increases the amount of charge required from the battery

itself, it also increases the number of cycles that the battery will undergo. The operation of these systems from a charge controller standpoint is beyond the control of the author as the devices were sourced from a proprietary manufacturer, and combined based on the recommendation of said manufacturer company. While the lifetime of this experiment will likely not result in the realization of these disadvantages, over the useful life of the components themselves, the SPSC battery will likely suffer an earlier failure.

Table 4.2: A summary of the data set from the SPSC station, including the parsed out complete strings and the quantity of identified Schedule Points found within each String.

Month	**Days**	**Length(Days)**	**Total**
June	7 - 30	24	101
July	1 - 5	5	23
July	15 - 31	17	52
August	3 - 31	29	83
September	1 - 7	7	25
September	14 - 30	17	6
October	1 - 5	5	0
October	7 - 15	9	0
October	17 - 23	7	0

4.4 Fall 2017 Weather Impacts on Data

The Fall of 2017 on the Colorado front range was ostensibly normal from a meteorological standpoint; however, the data sets from the Wilderness Place and SPSC stations display a sharp decrease in Solar irradiance in September not simply due to the lowering position of the Sun in the southern skies. The data from both stations display a chaotic Solar charging current throughout the month of September, with near zero charging on September 23, 24, and 27, the first two days constituting an early Fall snowstorm, and the last a complete cloud coverage day. As a result of this poor solar resource Fall, the quantity of Schedule Points sharply reduced in September, and became zero for the entire month of October at both stations. As the majority of this data analysis

occurs between Schedule Points, which are taken as clear indicators of 100% SOC, the bulk of the data sets from September and October has yielded a lack of useful data for the purposes of this work.

4.5 Operation of a Battery through the Day

Although a macro analysis of the entire data set to identify trends in the 'Battery Energy Efficiency' and 'Coulombic Efficiency' is the goal of this work, it will be well appreciated by the reader to receive an upclose analysis of the operation of the battery throughtout the daily operations. For this purpose, the voltage and current profile from the entire day of operation on June 6, 2017 at the Wilderness Place station is presented, along with a breakout of what the profiles indicate as far as battery operation. Fig. 4.5 provides the current and voltage profiles.

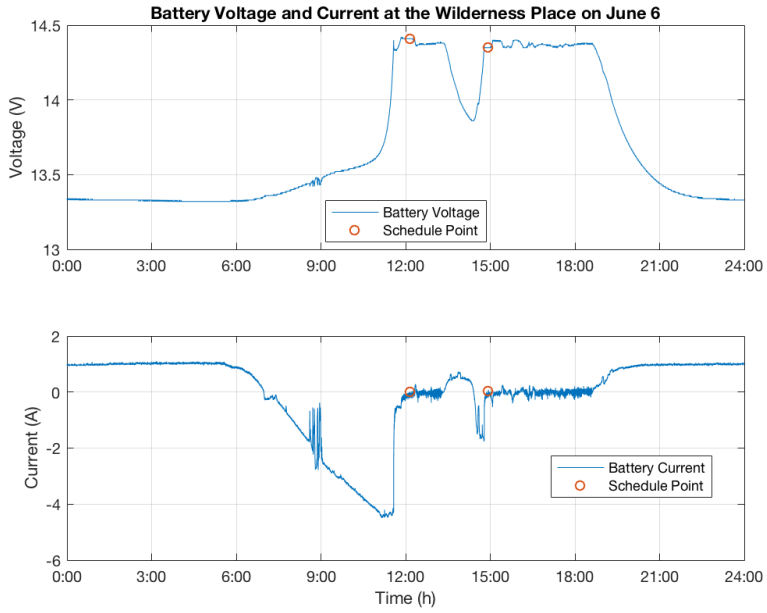

Figure 4.5: The voltage and current profiles througout the day on June 6, 2017 at the Wilderness Place station are presented for a brief analysis on the actual implications of the variety of outputs.

- **0:00 - 6:00:** Nightime; the continuous transfer of energy from the battery to load is evident in the positive current flow from the battery terminals. Notice the slight ramp in current

flow, coinciding with a slight decrease in voltage. This indicates movement on the SOC vs. OCV profile, and the counter action (current increase with voltage decrease) is necessary to maintain a steady power output to match the load consumption.

- **6:00 - 9:00:** As the sun emerges, the Solar PV panel begins to capture the resource and displaces the current flow necessary from the battery to power the load. The battery begins to charge (represented by negative current flow) as the solar resource grows. Variability in the resource is evident just before 9:00, likely due to passing cloud cover.

- **9:00 - 12:00:** The battery continues to charge at an increasing rate until a 100% SOC is achieved just before 12:00. Both state variables represent this point; the voltage rise exponentially in the final 30 minutes to approximately 14.4V at which point the BMS discontinues charging and the current drops to zero.

- **12:00 - 15:00:** Because the BMS has disabled charging through battery disconnection, as opposed to the charge controller disconnecting the solar resource, the current remains nearly steady at zero amps while the charge controller uses the solar resource to run the load. Mild chatter is evident as the battery is discharged to fill in mild shortfalls in the solar resource. Finally, around 1:30, the solar output is reduced to less than the load demand (likely cloud cover), and the battery begins to supply a non-trivial amount of energy. The result is a voltage drop and the start of a new battery cycle. Following the later onset of solar resource, the battery charges once more and reaches a 100% SOC at 15:00.

- **15:00 - 18:00:** The solar resource remains steady and the battery isn't discharged in an appreciable manner. As a result the voltage remains steady at 14.4V, and the current remains steady at zero amps.

- **18:00 - 24:00:** As night falls, the solar resource diminishes to zero and the battery begins to supply all energy required by the load. Initially, the voltage drops rapidly, until reaching a plateau value of approximately 13.4V for the evening.

4.6 Station Temperature

Figure 4.6 shows the temperature profiles for each day of August at the SPSC and Wilderness Place stations. Due to the location of these stations on the roof, they are susceptible to high temperatures throughout the day as the Sun's irradiation has an un-occluded path to the system containers. As the stations derive all energy necessary to operate from Solar PV, the bulk of charging occurs at higher temperatures because of the Solar irradiance patterns. There are subtleties within the temperature profiles that are discussed in Fig. 4.6, in addition to cross station corroboration. For instance, the two low temperature days (green and blue curves in both charts), show similar temperature profiles indicating appropriate calibration, as well as a low Solar resource day, because of the similarity in measurement at two locations separated by a few miles. Of note is the larger time span of higher temperatures recorded at the Wilderness Place station. Because of the location of the SPSC station near a large concrete wall directly to the west (see Fig. 3.6), direct heating from solar irradiation falls off rapidly in the early afternoon. As a result, the temperature at Wilderness Place remains much higher until later in the day.

Due to the temporal co-location of high station temperatures and LFP battery charging due to the availability of the solar resource, the shorter cycles experienced at either station are typically at much higher temperatures. For the case of the Wilderness Place station, which has a much different charging pattern as described in 4.2, this yields on average one high temperature cycle between the early morning SP and late afternoon SP, and then a low temperature cycle which extends from the late afternoon until the following morning. The resulting distribution of average cycle temperature versus cycle length, as shown in Fig. 4.7, is a near equity in the number of intraday cycles (less than 5 hours), to the number of interday cycles (greater than 20 hours). The different operational procedures at the SPSC station, that of a greater quantitiy of cycles during the midday hours because of the Solar curtailment default, yields far more cycles occuring at higher temperatures. In fact, while the Wilderness Place station achieves similar high temperatures throughout the day, the rapid cycling at the SPSC results in complete cycles occuring at higher temperatures because

Figure 4.6: The temperature profiles recorded at the stations of Wilderness Place and SPSC, Wilderness Place represented by the chart on the right. Of note, and expected, is the rapid temperature rise just as the Sun's irradiation strikes the rooftops circa 7:00 AM. Note the overall steeper temperature ascent of SPSC, due to a large HVAC system occluding the morning Sun, but only briefly. Additionally, although there is no southern protection which results in higher temperatures at the SPSC, there is a wall to the West of the system container which results in a more rapid temperature decline in the afternoon. In the case of the Wilderness Place, the early morning rays strike the system container directly, and result in the sharp knuckle at about 7:00 AM. A southern structure provides midday protection, and results in lower temperatures. The lack of a large western wall, as at SPSC, results in a longer stretch of higher temperatures. Note Figures 3.6 and 3.5 for station orientation.

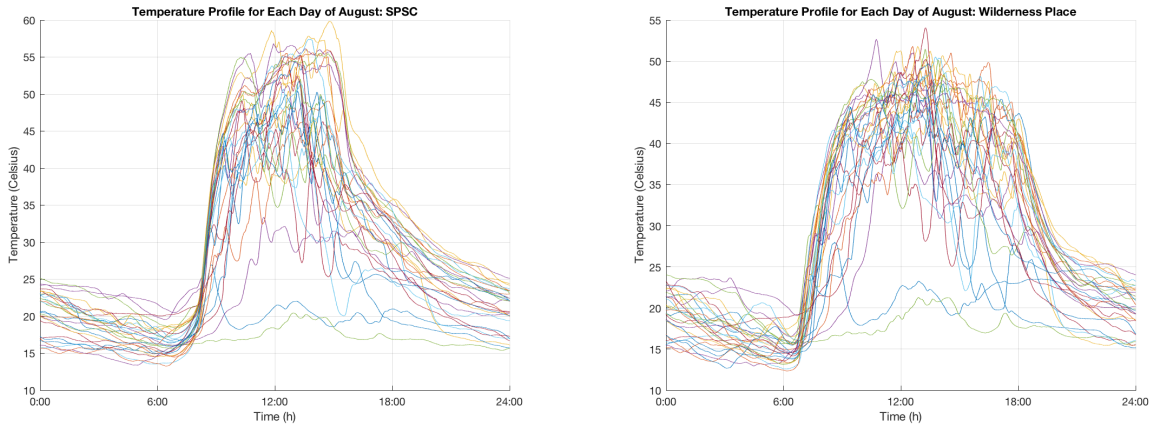

of the short cycle duration. The distribution of average cycle temperature verse cycle length at SPSC is also shown in Fig. 4.7.

Figure 4.7: An analysis of the average temperature during a cycle versus the length of the cycle. For those cycles under six hours, the solar resource decreased to the point of discharging the battery appreciably such that a full charge was again achieved before the end of that day's period of solar resource gain, much like the scenario described in section 4.5. As a result, these cycles are at a much higher average temperature.

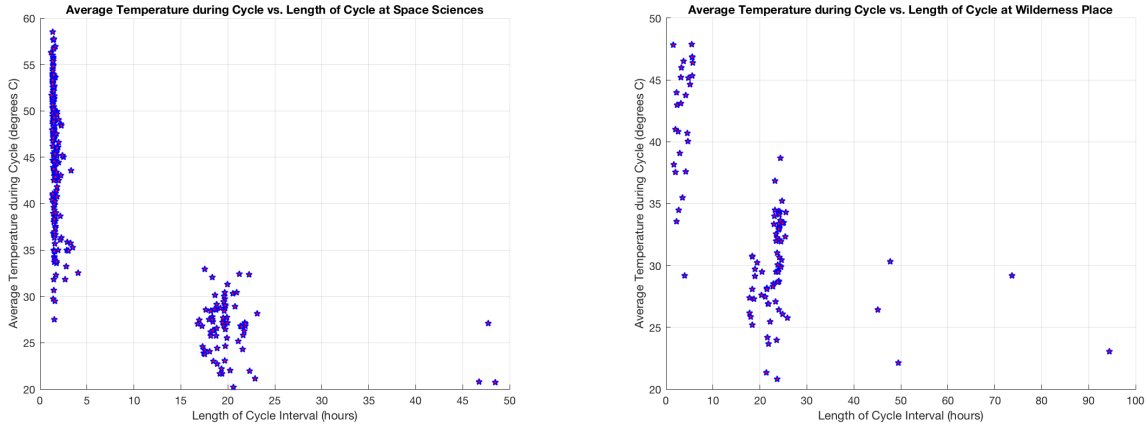

Chapter 5

Analysis

Now that the data has been cleaned and combed such that all Strings and Schedule Points are well defined, an analysis can begin to draw conclusions about the Coulombic Efficiency and Battery Energy Efficiency. Upon determining these factors, we can then draw conclusions about any drift in these values with respect to increased cycles of the LFP that may be indicative of capacity fade due to operation. It goes without any further comment that all power flow in this system is strictly DC, and as a result no consideration for reactive power flow is necessary. Before we go any farther, however, a brief discussion on the error propagation is necessary.

5.1 Error Considerations

As derived and summarized in Section 3, there are errors associated with the variety of microcontroller measurements, which are attached to each sample. Throughout the analysis, the measurements are typically summed over specified intervals, and it is therefore important to understand how this error propogates and grows through these intervals. Additionally, special regard is necessary for the power flow calculations, which is the product of two state variables each possesing their own error. First, we consider the error associated with the summation across an interval.

The process for determining the ampere-hour (Ah) discharge, or charge, is a simple summation of all of the discharge/charge currents measured, multiplied by an interval correction. It follows the simple form shown in Equation5.1, which is subscripted for discharge, where N equals

the number of discharge intervals.

$$Q_D = \Delta_i \sum_{n=1}^{N} i_D(n) \tag{5.1}$$

Here, the value of Δ_i is the temporal component representing the length of each interval, and $i_D(n)$ is the current discharge measurement. The removal of Δ_i from the summation is possible because it is a constant throughout the entire interval. The actual value of Δ_i is a constant throughout the entire experiment, and is represented as follows:

$$\Delta_i = 5sec \cdot \frac{1hr}{3600sec} \tag{5.2}$$

Because there is no error associated with this number, it can be factored out of the error calculations due to the condition now highlighted. According to [54], if $z = Bx$, where B is known exactly, then the error in q, δz, is:

$$\delta z = |B|\delta x \tag{5.3}$$

In our case, B represents Δ_i, which is known exactly, and can be removed from error considerations.

Let δq = the total error in the total charge/discharge $Q_{C/D}$, of the battery in an entire cycle. Let δx = the resolution error per sample of $i_{C/D}(n)$, and $N_{C/D}$ = the total number of charge, or discharge, intervals per cycle. According to [54], the total error in charge/discharge counting is then the Euclidean norm of all of the sample errors:

$$\begin{aligned} \delta_q &= \Delta_i \sqrt{\delta x_1^2 + \delta x_2^2 + ... + \delta x_N} \\ &= \Delta_i \sqrt{N(\delta x)^2} \\ &= \Delta_i \delta x \sqrt{N} \end{aligned} \tag{5.4}$$

Where all δx values are identical and represented by the resolution error of the current monitor. The calculation of total charge/discharge, including error, is then:

$$\begin{aligned} Q_C &= \Delta_i \sum_{n=1}^{N_C} i_C(n) \pm \Delta_i \delta x \sqrt{N_C} \\ Q_D &= \Delta_i \sum_{n=1}^{N_D} i_D(n) \pm \Delta_i \delta x \sqrt{N_D} \end{aligned} \tag{5.5}$$

The calculation of the Coulombic efficiency requires taking the quotient of the charge delivered and the charge recovered. Let $\delta d = \Delta_i \delta x \sqrt{N_D}$, $\delta c = \Delta_i \delta x \sqrt{N_C}$, and $CE = Q_D/Q_C$. According to [54], the error in this calculation, represented as δCE, is equal to:

$$\delta CE = |CE| \cdot \sqrt{\left(\frac{\delta d}{Q_D}\right)^2 + \left(\frac{\delta c}{Q_C}\right)^2} \tag{5.6}$$

To calculate the energy delivered/recovered of the batteries, the summation of the product of the current and voltage measurements with the time interval must be calculated. Namely, for the case of energy delivered

$$E_D = \sum_{n=1}^{N_D} \Delta_i \cdot i_D(n) \cdot v_D(n) \tag{5.7}$$

Where $i_D(n)$ is as identified previously, and $v_D(n)$ is the voltage across the battery during the discharge interval. The error associated with this measurement, according to [54], is:

$$\delta E_D = \Delta_i \sum_{n=1}^{N_D} \sqrt{\left(\frac{\delta x}{i_D(n)}\right)^2 + \left(\frac{\delta y}{v_D(n)}\right)^2} \tag{5.8}$$

where δx is the associated current measurement error, and δy is the associated voltage measurement error. Unfortunately, the step by step product of these measurements doesn't allow any gross simplifications as in the determination of the Coulombic efficiency because the values are changing throughout the summation interval.

5.2 System Efficiency

The power electronics that manages the power flow between the Solar PV, the LFP batteries, and the Load has associated inefficiencies on account of power consumption during operation. A small laboratory experiment highlighted in Section 3.2.2 was performed to understand the consumption of the charge controller when only managing the LFP/Load interaction. A minimal power consumption in this configuration was found; however, this operation isn't expected to yield substantial inefficiences, unlike the MPPT and subsequent power derivation from the Solar resource. Consider the system power flow diagram in Fig.5.1.

Figure 5.1: The following shows the adopted power flow convention and associated efficiencies between the Solar Photovoltaic panel (Renewable Energy Source (RES)), the Lithium Ferro Phosphate battery (Energy Storage System (ESS)), and the Load. These three devices are managed by the MPPT Charge Contoller, which consumes a certain amount of power for management between any of the three devices. Shown are the symbols representing efficiencies and power flow from each respective device.

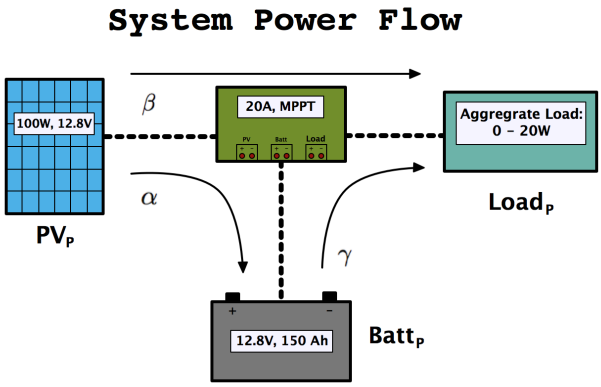

To derive the efficiency factors from the data, we must first state the relations. For the case of sufficient solar irradiance such that the Solar PV powers the load and charges the battery, we have the following:

$$PV_P = \frac{Load_P}{\beta} + \frac{Batt_P}{\alpha} \tag{5.9}$$

which can be approximated as:

$$\alpha\beta PV_P = Load_P + Batt_P \tag{5.10}$$

because it was found in the laboratory that the efficiency in sourcing power from the LFP battery to the load was near 100%.

In the event that the Solar PV is supplying power, but only a portion of the amount needed to drive the load and none to charge the battery, the following relation exists:

$$Load_P = \beta PV_P + \gamma Batt_P \tag{5.11}$$

The relation from Equation 5.11 only occurs at the Wilderness Place station, where the charge controller discontinues the charging of the battery upon reaching a Schedule Point, and then operates the load with the Solar PV resource supplemented by the LFP. This relation does not occur at the SPSC station, where the Solar PV resource is completely curtailed upon the LFP reaching a 100% SOC.

If there is no irradiance, i.e. it's nighttime, or for the case of SPSC, the LFP battery reaches a 100% SOC and then begins powering the load exclusively, we have:

$$Load_P = \gamma Batt_P \tag{5.12}$$

which is the equivalent of the laboratory derived efficiency in which the controller is managing the power flow from the battery to the load, found to be near 100% at room temperature under comparable load consumption.

5.2.1 Overall System Efficiency

Before deriving the relationships between individual components of the system, we can calculate an overall system efficiency quite readily by taking the ratio of energy delivered to the load divided by the energy derived from the Solar resource, as shown in Equation 5.13. Using the Schedule Points identified within the data sets, an overall cycle efficiency has been calculated for each

cycle between the SPs.

$$\eta_{system} = \frac{E_{load}(c)}{E_{solar}(c)} \tag{5.13}$$

where c is the cycle number under investigation, as determined between two schedule points. Figure 5.2 shows the overall efficiency results at the Wilderness Place station as a function of cycle number. Note, an accurate measurement of the Solar PV production was not possible until after upgrades to the system were performed, and the results is that an overall efficiency calculation isn't possible for the first 120 cycles. Subsequently, the station was relocated from its prior location to the Wilderness Place location where the Solar PV panel was supplanted by a 100W panel, as opposed to the 140W initial panel. The entirety of the data plotted in Fig. 5.2 is with the 100W panel.

Figure 5.2: The overall system efficiency at Wilderness Place verse cycle number. As defined in Equation 5.13, this metric contains the battery performance, but it is embedded amongst other system factors. A slight drift towards lower efficiencies with a greater number of cycles is present, but not well defined.

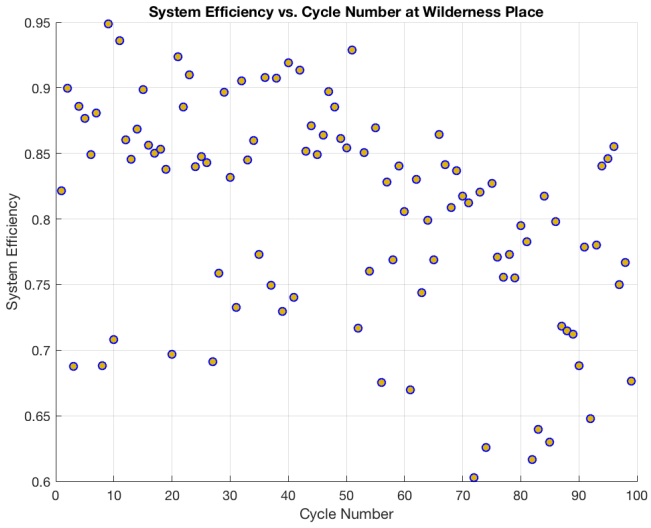

The distribution and spread of the data in Fig. 5.2 doesn't lend itself to any easy conclusions. In fact, the data seems to represent two different sets partitioned into cycles 1 - 50, and 50 - 100. The only change at this station through this portion of the experiment, which did occur around cycle 50, was a slight reduction in load when a radio was removed from the station. A slight load consumption reduction of about 10% ensued; however, this should only impact the C-rate of

discharge as the efficiency is normalized, meaning the decrease in energy consumption should be matched by a decrease in energy harnessed. Due to the large capacity of the Wilderness Place LFP battery, the reduction in load equates to a change from 0.0066C to 0.006C. Regardless, the overall system efficiency shows a wide range from nearly 95% all the way down to 60%.

To further define any deviations in conditions around the overall system efficiency, Fig. 5.3 shows the efficiency with respect to cycle length(on the left), and temperature(on the right). For the case of cycle length, there is a clear disparity between the efficiency regime of the intraday cycles (60% - 80%), and the interday cycles (70% - 95%), where there is no overlap between the lower, and upper, 10% of each regime, respectively. As previously discussed in Section 4.6, there is a clear relation between the shorter cycles and higher temperatures due to the charging/cycling tendencies of the systems during the day, while temperatures and sun exposure are greater. The second chart of Fig. 5.3 shows the distribution of system efficiency with respect to temperature. Although still too broad of a distribution to make any conclusions, there is a more distinct decrease in efficiency with higher temperatures as opposed to verse cycle length.

Figure 5.3: Plots of the overall system efficiency at the Wilderness Place station. On the left is overall efficiency versus cycle length, showing a large distribution for all intervals (sub day, overnight, multiple days), but a general reduction in efficiency during shorter intervals. On the right is the overall efficiency verse temperature. While still quite scattered as in Fig. 5.2, a general trend toward declining efficiency with temperature is present.

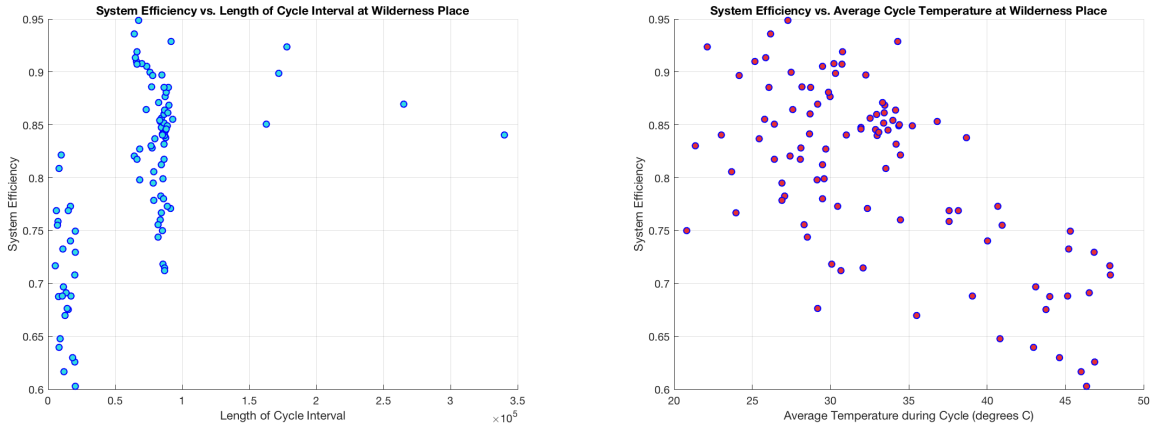

Figure 5.4 shows the overall system efficiency at the Space Sciences station. The cause

for three times as many cycles is due to the many, short cycles that occur during the day while the solar resource is available; because the SPSC system curtails Solar upon reaching a 100% SOC, the battery experiences many more cycles in a single day than the Wilderness Place system. Particularly surprising with the SPSC overall efficiency dataset is the much tighter distribution at higher efficiencies as compared to the Wilderness Place system. Not only is the bulk of the data contained within 85% - 98%, there is a slight decrease in the overall system efficiency, which may be indicative of the LFP battery showing a decrease in Coulombic/energy efficiency. Although the overall system efficiency doesn't account for the efficiency of the battery explicitly, decreases in battery efficiency will manifest itself in overall system efficiency decreases as a greater amount of energy is required to charge the battery for a set amount of load consumption.

Figure 5.4: The system efficiency at the SPSC vs. Cycle Length, as defined in Equation 5.13. Unlike the results of the same analysis for the Wilderness Place in Figure 5.2, the system efficiency at SPSC shows a tight gathering around 95%.

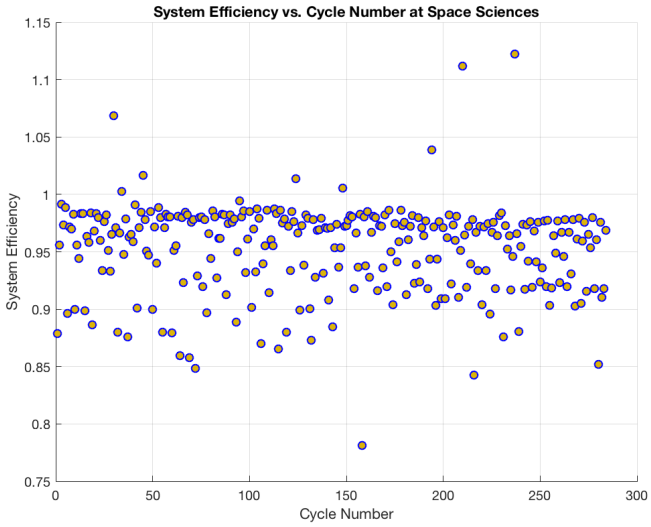

The plots of overall system efficiency verse cycle length and temperature are shown in Fig. 5.5. The intraday cycles show a wide range of efficiency values encompassing the majority of the spread prevalent in fig. 5.4, whereas the interday and multi-day cycles show a very close bunching around 96% - 98%. Interestingly, the greater than parity efficiencies occured at mid-average temperatures, as shown in the chart on the right of Fig. 5.5. Immediately after this temperature, the range

of efficiencies expands enormously, indicating a high temperature, or short cycle influence on the overall system efficiency.

With respect to temperature effects, the system is expected to be less efficient at higher temperatures due to power electronics sub-optimal operating regimes, and the battery efficiency itself decreasing due to a greater number of side reactions. Additionally, the current monitors are susceptible to greater error and non-linearity influences at higher temperatures. Regarding the short cycles, the rapid charge/no-charge shifts prevalent throughout the day at the SPSC station could have impacts on the data capture due to the average nature of the Arduino, and the Schedule Point identification algorithm. While this isn't expected to cause a lower effieciency itself, it may explain part of the wide range in derived efficiencies during the shorter cycle lengths.

Figure 5.5: Plots of the overall system efficiency at the SPSC station. On the left is overall efficiency verse cycle length, showing a large distribution for the intraday cycles, but a tight bunching of efficiencies during interday and multiday cycles. This large distribution during the cycles of similar length indicates that the short cycle itself is not responsible for the large fluctuations. On the right is the overall efficiency verse temperature. This chart shows a break from the tight distribution at low temperatures, to a large distribution at high temperatures marked by the greater than parity outliers around 35 degress C.

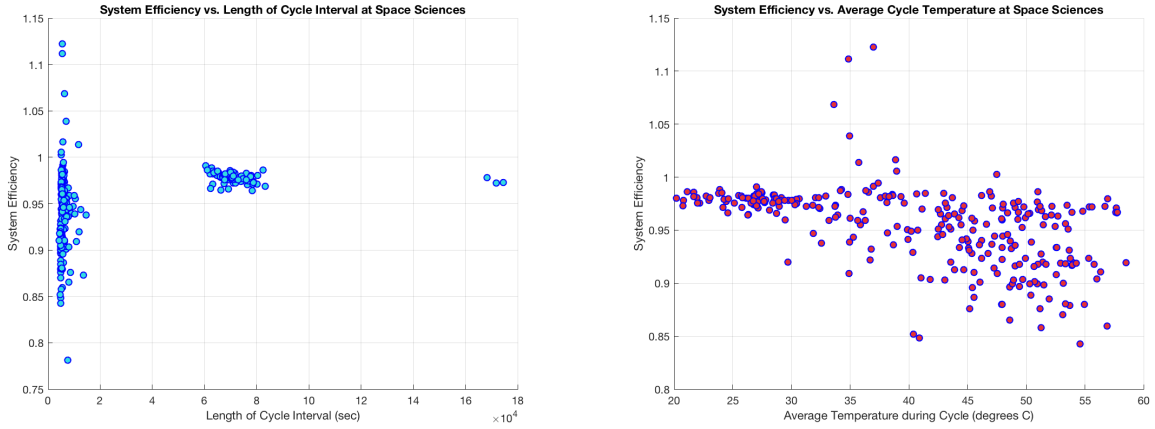

5.2.2 Charge Controller Efficiency

To derive the charge controller efficiency in supplying Solar PV power to the Load and Battery as required, namely $\alpha\beta$ from Equation 5.10, the data was parsed to identify the total power consumption of the system only when the Solar PV was supplying power. The datasets derived from the Wilderness Place and SPSC datasets are both depicted in Fig. 5.6, verse cycle length.

Figure 5.6: The charge controller efficiencies in managing the power flow from the Solar resource to the Load and LFP battery. On the left is the Wilderness Place distribution, while the SPSC distribution is on the right. These are derived by the dataset by neglecting all data points when the Solar resource is not present. The distributions are similar to the overall system efficiency, which was expected due to the the near parity efficiency between the battery and load while no solar resource is available.

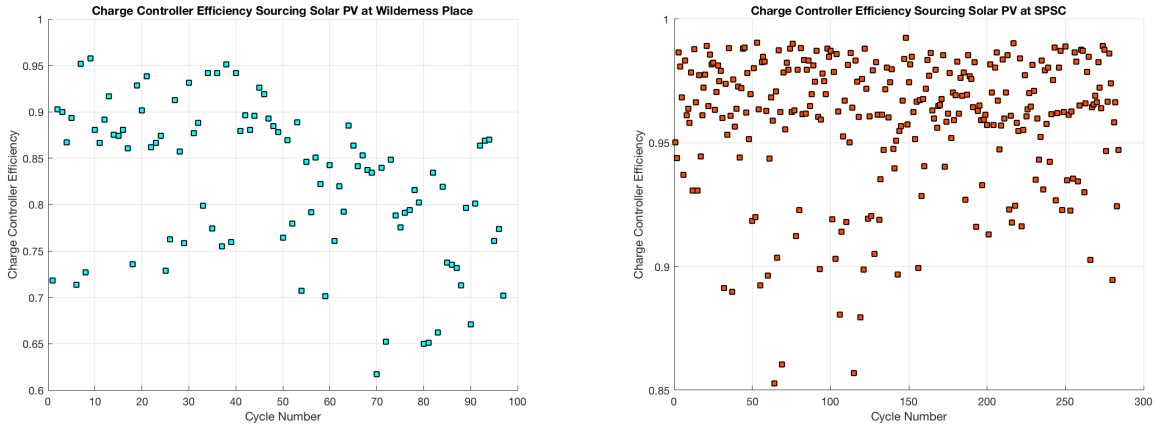

The resultant efficiencies are as expected, i.e. they are near the overall system efficiencies because the other predominant operational condition is the controller simply managing power flow between the battery and load, which was found to be near 100% in the laboratory prior to deployment. As a result, the charts closely resemble those of Figures 5.2 and 5.4.

5.2.3 Battery/Load Power Flow Efficiency

As a final attempt to equate the high efficiency in power flow from the battery to the load through the charge controller as measured in the laboratory, all data points during which no Solar

resource was present for the previous 30 minutes were extracted and an efficiency derived. The purpose of waiting for a clear presence in no Solar resource was to ensure that the lack of Solar wasn't due to rapid irradiance fluctuations. The results yield a power flow efficiency resembled in Equation 5.12 as γ.

Figure 5.7: The results of charge controller efficiency analysis while no Solar resource is present. Although both distributions are near 100% as expected, the rising trend of the Wilderness Place data set with respect to temperature is the opposite of expectations, while the SPSC declining trend was anticipated.

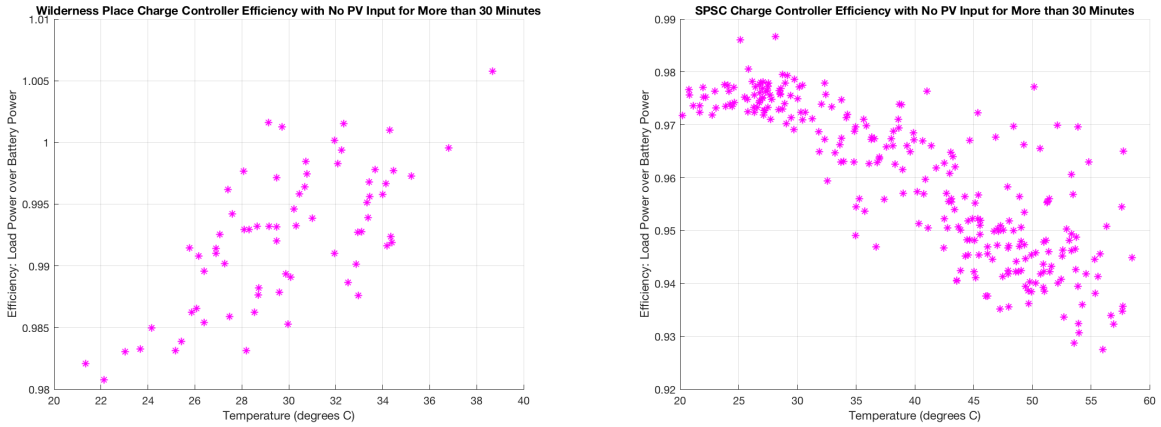

Figure 5.7 shows the results of the γ derivation plotted against the average temperature throughout the interval of interest. As expected, both of these show a near 100% efficiency as found in the short laboratory test. Of surprise is the presence of opposing trends between the data from Wilderness Place and SPSC stations. The decrease in efficiency with higher temperature as evident in the SPSC set is expected due to the increased power consumption of the charge controller at higher temperatures. The larger spread in efficiencies may be on account of the higher temperatures influencing the data capture. What isn't readily explainable is the increase in efficiency of the Wilderness Place. There is no clear reasoning or indication for this trend. However, there is the likelihood that the higher temperatures occurred over shorter intervals, which could indicate a potential data issue.

5.3 State of Charge and Coulombic Efficiency

The State of Charge (SOC) of a battery is defined as the quotient of the capacity remaining and the total capacity at full charge, i.e. the SOC at a time t after discharge begins is:

$$SOC(t) = \frac{Q_{full} - Q_{delivered}(t)}{Q_{full}} \times 100\% \tag{5.14}$$

where Q_{full} represents the capacity, in ampere-hours, at full charge, and $Q_{delivered}$ represents the delivered charge, in ampere-hours, since the initial deviation from Q_{full}.The process of tracking the charge delivered by the battery pack is known as 'Coulomb Counting'. While sounding obscure at first, simple consideration of the units of ampere, namely $[C]/[s]$, reveals that by tracking current flow with respect to time, the resulting quantity is of units, Coulombs. The following is the mathematical equivalent:

$$Q_{delivered/received}(t) = \int_{t_0}^{t} \eta_{C/D} \cdot i_{battery}(t)dt \tag{5.15}$$

where t_0 represents the point in time of the initial deviation from Q_{full}, and $\eta(t)$ represents the 'Coulombic Efficiency' that was introduced in Equation 2.8. During discharge, η_D is taken as one to serve as the benchmark to which the efficiency is defined; however, during charge, η_C is less than one and it is the goal of this work to identify the Coulombic efficiency and a drift therein throughout the life of the batteries through the data set. The point at which Q_{full} is determined and t_0 is identified is known as a 'Schedule Point', which were described in Section 4.1 and have been used thus far in the calculations of efficiency. In tracking the SOC during a charge cycle, knowledge of the Coulombic efficiency is evidently required.

5.3.1 Wilderness Place Coulombic Efficiency

With the Schedule Points well defined through the identification algorithm and a clear understanding of what the Coulombic efficiency represents, the derived Coulombic efficiency for the Wilderness Place station is now presented with associated error, derived via the methodology outlined in section 5.1, in Fig. 5.8. Of immediate note is the obvious data set shift at approximately

120 cycles, which is the point of data collection at which the station was relocated from the South Complex where a 140W Solar PV panel was in use, to the Wilderness Place station where a 100W panel was in used. Due to this shift, as highlighted in section 4.2, the operation of the system switched from many intraday cycles to one of, on average, one intraday cycle per day. Simply noting this change, it can be guessed that the majority of the low efficiency points are from the intraday cycles.

Figure 5.8: The Coulombic efficiency as derived from the Wilderness Place dataset inbetween Schedule Points.

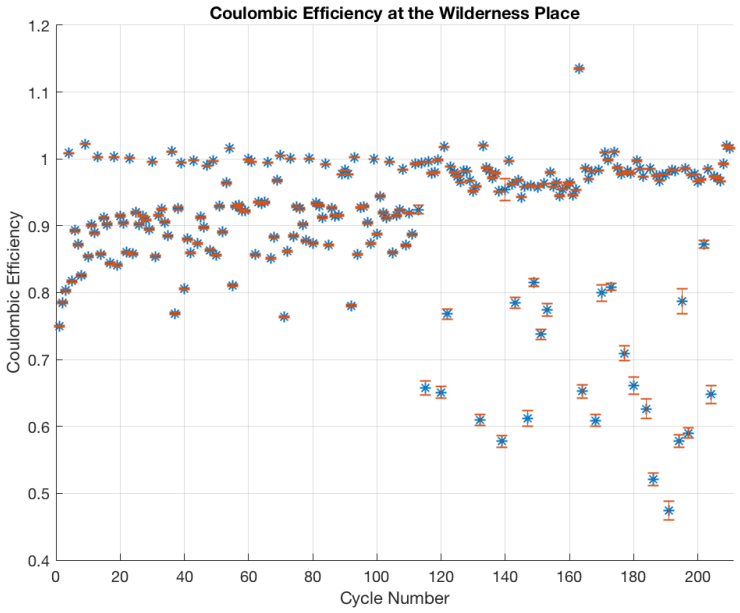

The error bars present incorporate the resolution error of the battery current monitor, as well as the 1.5% error as noted in the specifications of the device. Although a value near one is expected, it isn't necessary to consider data with error well beyond this value of one as deviant or useless due to the many other factors that may contribute to variance. Beyond the temporal aspects, which may cause issues in Schedule Point identification or microcontroller error, there is the high average temperature characteristic of shorter intervals. High temperature is expected to cause deviations in the Coulomb efficiency and is addressed in a later section.

To provide more insight into the circumstances surrounding the large discrepancies in Coulom-

Figure 5.9: The Coulombic Efficiency as determined for each complete cycle between Schedule Points, first with all cycles shorter than 2 hours removed on the left, and then for only cycles exceding 6 hours. The resultant distribution on the right contains only interday and multiday cycles. A linear regression best fit line is included to show the negative trend in Coulombic efficiency, although the decay with respect to cycle number isn't expected to be linear due to the variability in system operation and environmental factors.

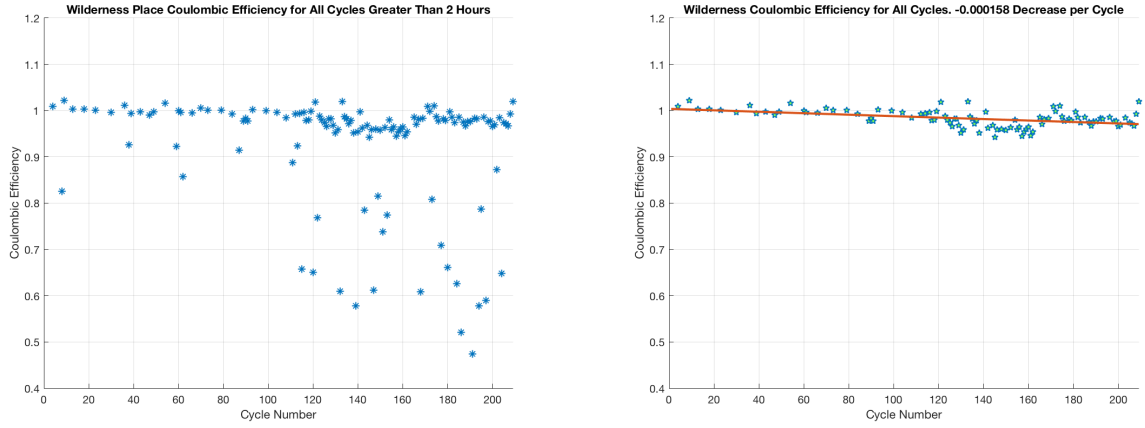

bic efficiency, Fig. 5.9 presents the same data set three times, filtering out first all cycles less than 2 hours long, and then all cycles less than 6 hours long. In the case of removing all cycles shorter than 2 hours, all of the rapid intraday cycles, present before station relocation are absent, but the longer intraday cycles post relocation are still present, as evident in the second chart. Upon the removal of all cycles shorter than 6 hours, the data set is a much tighter distribution just below one. At this point, the data set only consists of interday cycles, during which the length of discharge is on average more than five times greater than the length of charge. Due to the discussion about the effect of error on Coulombic efficiency in section 2.6, we see that the non-linear effects due to denominator(total charge) error have far less influence than the linear effects of the numerator (total discharge) error.

For the scatter plot containing only cycles greater than 6 hours in Fig. 5.9, an ordinary least squares linear regression fit was taken and the decay constant presented in the title of the plot. With these long cycles, a much tighter distributiion around one is present, indicating that the variance in both the numerator and denominator are small. As such, a linear regression is appropriate given the linear relation with small deviations as shown in section 2.6. The fit isn't

precise, which is acceptable because it is only there to serve as an indication of a negative trend in the Coulombic efficiency over many cycles. The derived factor is a decrease of 0.00016 in Coulombic efficiency per cycle, which is reasonable considering the expected life of the LFP batteries. Factors influencing the lack of a precise fit include varying temperatures over all cycles, depths of discharge, and charge rates due to the solar resource.

5.3.2 Space Sciences

The results of the SPSC Coulombic efficiency analysis are shown in Figures 5.10 5.12. An analysis identical to the approach for extracting the same information from the Wilderness Place station was used. Of surprise is the bias error througout the duration of all 284 cycles captured that results in an efficiency greater than 100%. This is a violation of the conservation of energy which indicates that there must be other factors unaccounted for, or unknown sources of energy within the system. The most likely case is simple measurement error, which is addressed first.

Figure 5.10: The SPSC Coulombic Efficiency with projected error based on the error calculation approach described in Section 5.1.

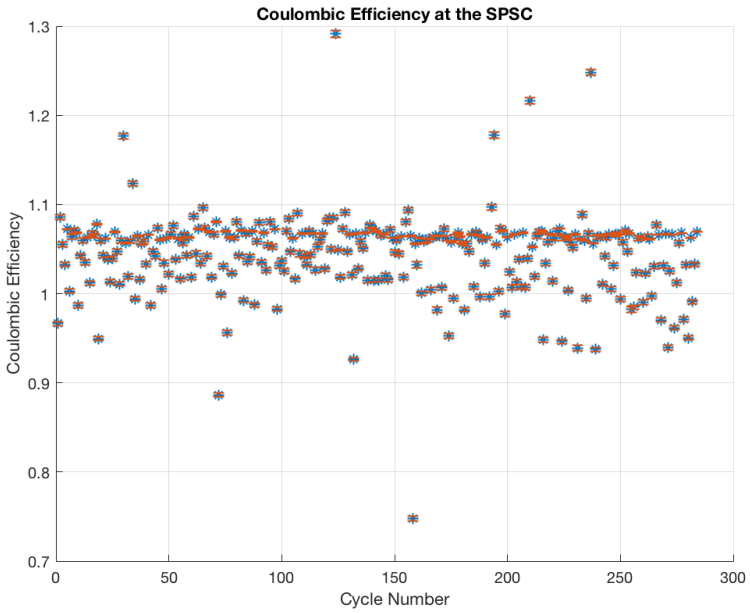

Figure 5.11 shows the bias error per cycle necessary to raise the Coulombic efficiency above

one, normalized to the number of samples in that cycle. Namely:

$$\delta_{Bias} = \frac{\Delta_{Bias}}{N_{samples}} = \frac{|Q_{Discharge} - Q_{Charge}|}{N_{samples}} \tag{5.16}$$

Figure 5.11: The minimum bias error per current measurement sampe required to rectify the greater than 100% Coulombic efficiency at the SPSC, as defined in Equation 5.16. The average per cycle is 0.058 A, which is twice the resolution error of the current monitor.

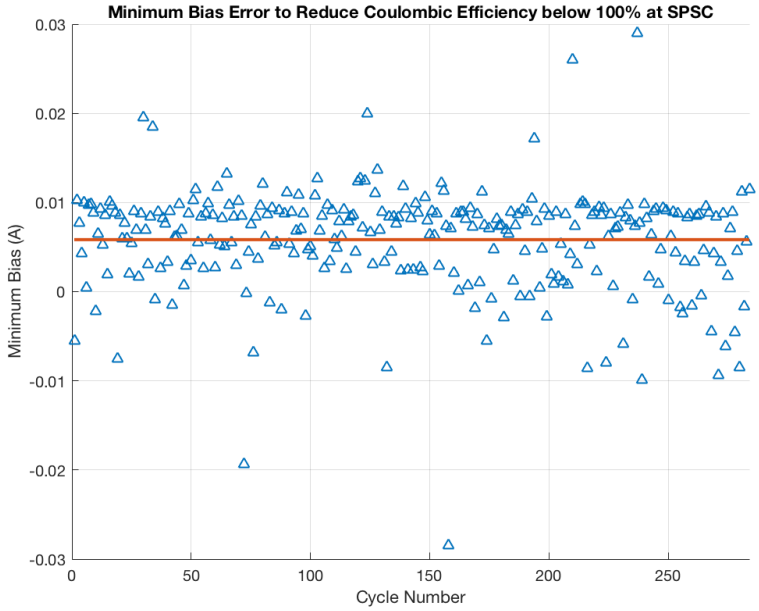

The average of the bias errors across all cycles was taken and found to be 0.058 mA, which is shown in Fig. 5.11. This bias is error is twice resolution error calculated for the battery current monitor at 0.029 mA. As such, following the robust calibration methods employed, it is unclear where this large and persistence error would have arisen. Regardless, although the values themselves are in error, it is reasonable to ask if a negative trend is still identifiable. Let $Q_{Discharge}$ and Q_{charge} represent the actual values of total charge delivered and recoverd, respectively. It follows that the results captured are represented by the addition to these two values of $N_D\delta_{X,Bias}$ and $N_C\delta_{X,Bias}$, where N_D and N_C are the quantity of discharge and charge samples in a cycle, respectively, and we have assumed the bias error to be constant at all times. The Coulombic efficiency is then:

$$\eta_{CE} = \frac{Q_{Discharge} + N_D\delta_{Bias}}{Q_{Charge} + N_C\delta_{Bias}} \tag{5.17}$$

The low discharge rate as compared to the larger average charge rate results in N_D being on average ten times greater than N_C, and therefore it is expected that the Coulombic efficiency results would be larger than actual with a bias error. However, identifying drift in the Coulombic efficiency is based on a growing quantity of charge required to reach a 100% SOC with respect to the quantity of discharge. Thus, although the bias error results in a greater than parity effficiency due to the values greater than one, a negative trend is nonetheless expected. Figure 5.12 shows the results of the trend present in cycles exceeding six hours.

Figure 5.12: The Coulombic efficiency at the SPSC station for longer cycles; all greater than two hours on the left, and all greater than six hours on the right. As previously discussed, there is significant bias error resulting in an efficiency greater than one. Regardless, it has been determined that a negative trend in the data is still expected, and the plot on the right exhibits slight decrease with cycle number.

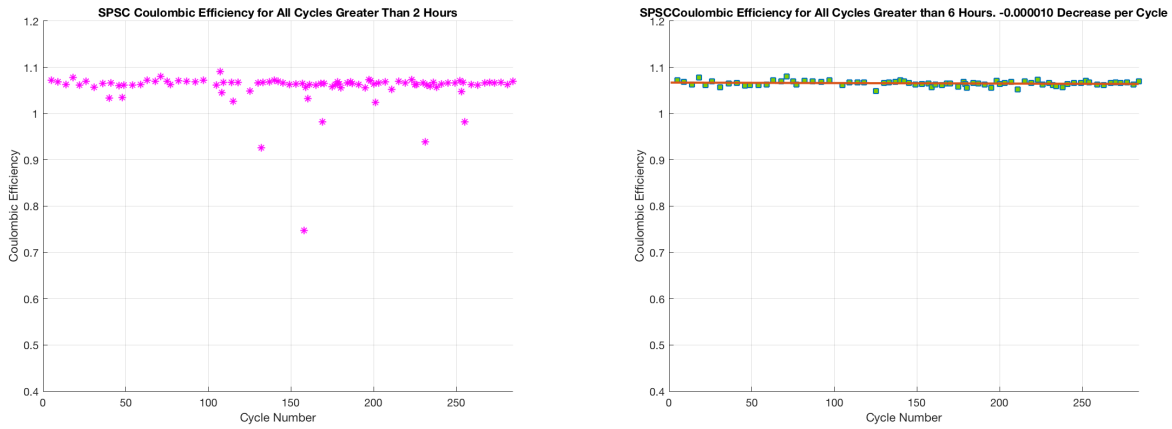

Another possible source of the error comes in the form of a net discharge from the LFP battery. That is, if the battery is degrading such that a portion of each cycle represents the operation of a primary battery in that no recharge capacility exitsts, than the Schedule Points will still be triggered by over voltages, but the full charge as compared to previous capacity will not be recovered. Figure 5.13 shows the results of the summation of the net discharge error as a function of cycle number, with a capacity mark at 200 Ah, representing the nameplate capacity of the SPSC LFP battery pack. It is immediately obvious that the net discharge resulting in Coulombic efficiencies greater than one has not exceeded even half of the capacity of the LFP pack. Thus, it

cannot be immediately stated that the battery is not defective and sourcing energy as a primary pack.

Figure 5.13: The Net Discharge of the SPSC battery. This is still well below the capacity of the battery itself, with a capacity of 200 Ah, and as such this theory cannot be ruled out by data analysis alone.

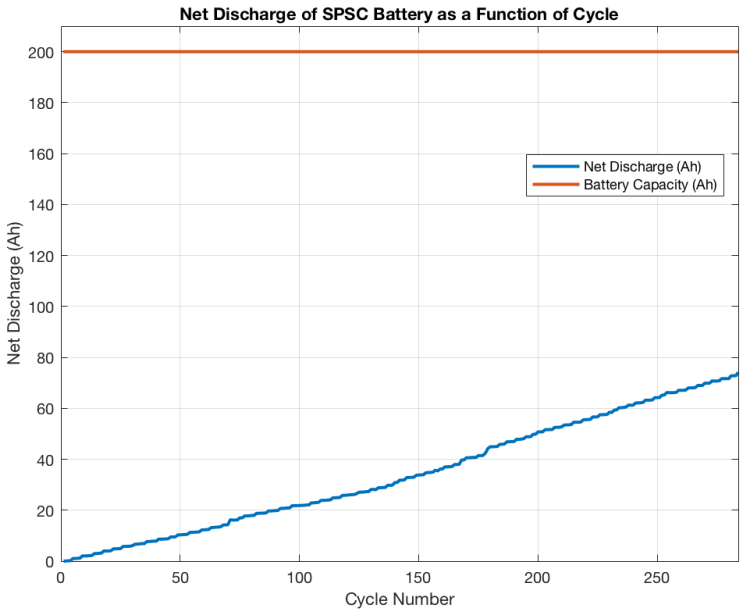

To pass judgement on this theory, the SPSC battery was retrieved from the station at the beginning of November, 2017, and a full capacity measurement was made in which the pack was fully cycled with a discharge at 0.06C, and then charged with CCCV. The resultant capacity of the SPSC LFP was $191Ah \pm 2Ah$, where the manufacturer specified capacity is 193Ah for the 200Ah pack, a value corroborated in initial capacity measurements. Therefore, it can be ruled out that the pack may be operating as a primary battery pack.

5.4 Temperature Effects

The literature discusses a strong relation between high ambient operational and storage temparatures to greater rates of degradation[61, 48, 57]. As discussed in Section 2, at higher temperatures a greater quantitiy of side reactions are expected to occur during the charge and discharge process due to the Arrhenius relation, shown in Equation 5.18.

$$k = Ae^{-E_a/(k_B T)} \tag{5.18}$$

where k is the rate constant, A is a pre-exponential factor, E_a is the activation energy, and k_B is the Boltzmann constant. It is apparent that higher temperatures cause an increase in the rate constant, which manifests itself as a greater number of side reactions and a decrease in Coulombic efficiency is expected. Fig. 5.14 shows the results of Coulombic efficieny plotted against the average temperature per cycle for the Wilderness Place.

Figure 5.14: The Coulombic Efficiency verse the average temperature during the cycle. While this shows a tight distribution near one with only a slight decrease with temperature until 35 degrees C, the distribution decays completely at temperatures greater than 35 degrees C.

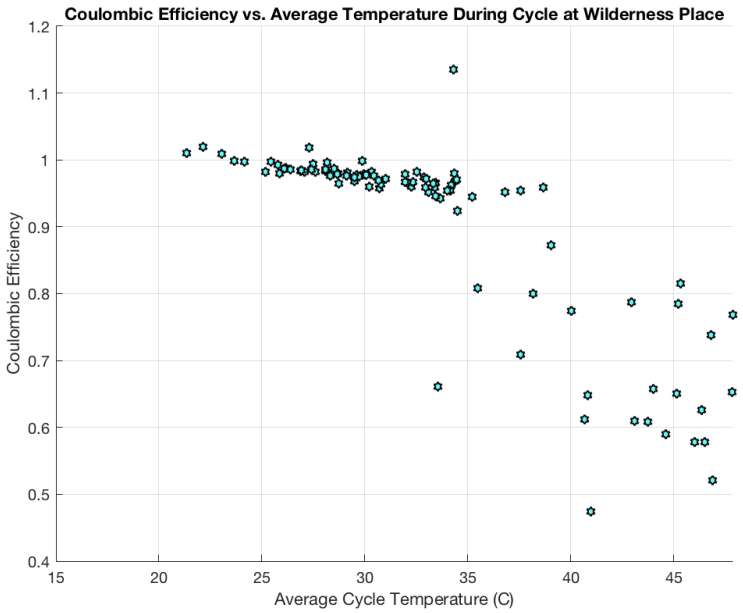

The slight decrease in efficiency present from 20 to 35 degrees C is expected and well defined.

The abrupt increase in variety of Coulombic efficiencies after 35 degrees C is suprising. Multiple factors beyond the LFP battery itself may be to blame. For instance, these high temperature cycles have already been shown to occur intraday, with shorter cycle lengths. Additionally, the monitoring electronics may be susceptible to large inaccuracies at higher temperatures. It should be noted that while the Wilderness Place station was relocated, this entire data set is only from post relocation data capture because an operational temperature sensor was not implemented until after the movement.

Figure 5.15: The Coulombic efficiency verse temperature at the SPSC station. Although this efficiency is greater than one and thus a large bias error is present, it has been previously noted that a trend is still reliably extractable and thus, a brief analysis is warranted.

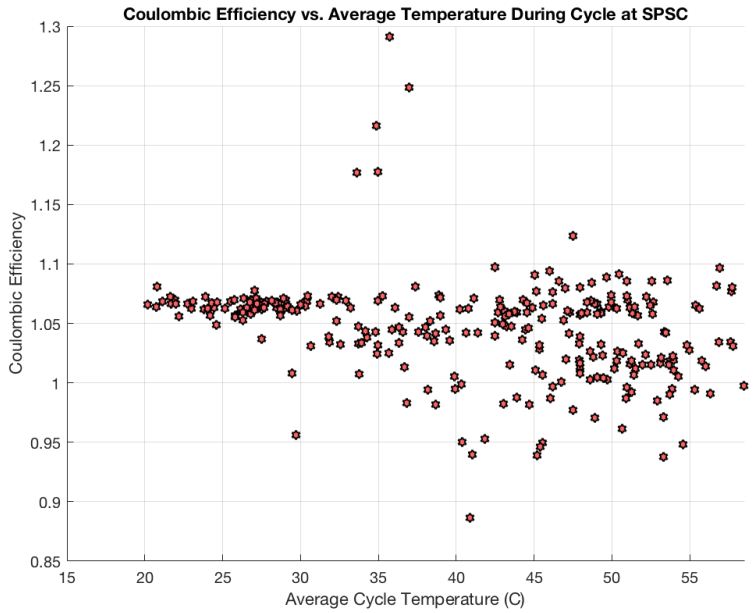

Figure 5.15 shows the Coulombic efficiencies per cycle plotted against temperature for the SPSC station. Although the large bias error forcing the resultant Coulombic efficiencies to values exceeding one is still obvious. Of note is the tendency towards well defined efficiencies at low temperatures, and a large spread resulting at high temperatures. Similar to the results of the Wilderness Place data set, the break up of the well defined data set occurs around 35 degrees C. Contrary to the Wilderness Place set, the SPSC data only shows an approximate 15% spread,

whereas the Wilderness Place set shows a spread in excess of 50%.

Figure 5.16: The Coulombic efficiency plotted against measured temperature at the SPSC station. The multiple intraday cycles are partitioned to reflect any internal system container temperature trends.

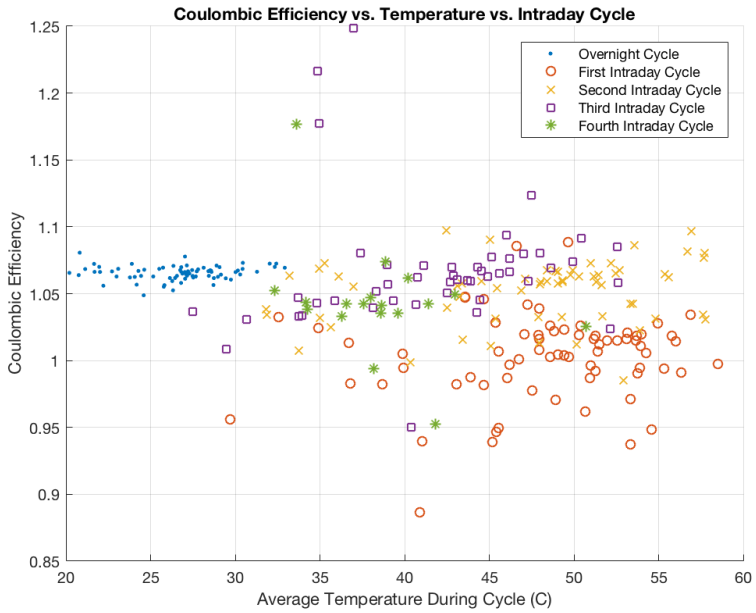

The operation at the SPSC station results in many intraday cycles. As a result, many cycles occur at high temperatures, but due to the location of the battery in the center of the station container below the control board, it is possible that there is a differential between the measured, and actual battery temperatures. To identify this differential, the intraday cycles have been identified temporally, and plotted vs. temperature in Fig. 5.16. The overnight cycles involved the greatest amount of charge recovery, but also occur at lower average temperatures not only because of the temporal location at the beginning of the day, but the long cycle length serves to nullify the higher temperature influence of the morning on the average cycle temperature. The first intraday cycle displays a tendency to lower Coulombic efficiencies (with respect to the other cycle results), regardless of the average cycle temperature. The latter day intraday cycles show a tighter distribution to the steady Coulombic efficiency of the overnight cycles. There is an expected heat generation due to i^2R losses, which will be largest at the high charging rates; but, the greatest

charging currents experienced are about 8 amps, at which rate heat loss of only tens of watts could be expected due to the LFP still charging at a rapid rate (indicated by the rapid ascension to 100% SOC) and the wattage the panel being only 140W. It is then not expected that internal heating is a factor contributing to the high system temperatures.

5.5 Battery Energy Efficiency

The Battery Energy Efficiency (BEE) was introduced in Equation 2.9. It has already been explained why the energy efficiency ought to be less than the Coulombic efficiency for chemistry reasons, namely the overpotential necessary for charging, and the underpotential resultant from the voltage drop across the internal resistance during discharge. It has also been explained in Section 2 why the BEE is expected to decrease with age due to the increasing internal resistance. In calculating the BEE per cycle, the sum of the product of the voltage and current flow through the LFP pack is taken during the charge and discharge portions of the cycle. The result is similar to the Coulombic efficiency due to the integration of the current flow, but it deviates due to the additional voltage factor. The error is necessarily larger due to the resolution error in the voltage measurements.

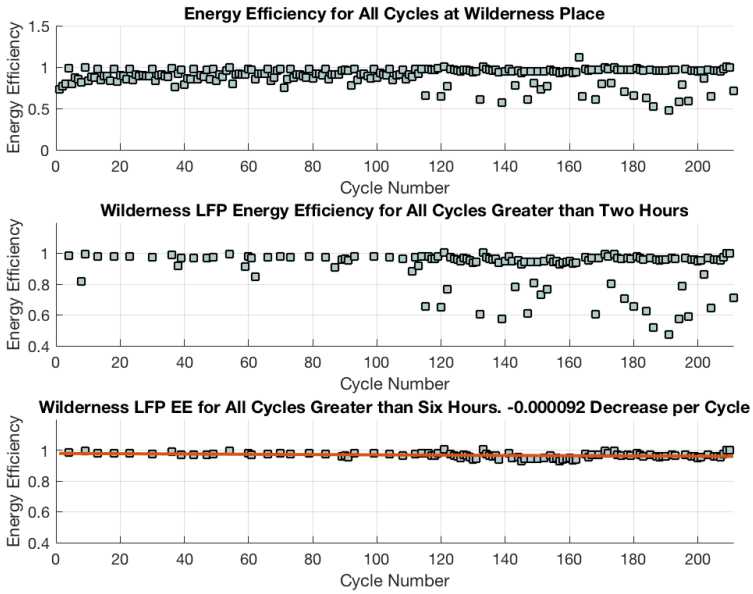

Figure 5.17: The energy efficiency vs. cycle number at the Wilderness Place station. A similar approach from the Coulombic efficiency is adopted in which the data is filtered in favor of longer cycles. A small net decrease per cycle is found for cycles exceeding 6 hours.

Figure 5.17 shows the resultant BEE calculated for the SPSC LFP battery through all cycles.

The result is very similar to the Coulombic efficiency due to the embedded Coulomb counting in the energy derivation. A greater decrease in the energy efficiency, as compared to the Coulombic efficiency, is expected due to the growth of the internal cell resistance, which will consume more energy without increasing the requisite current flow. With the linear fit on the final plot of only cycles greater 6 hours, we see that the decay rate is only half that of the same derivation for the Coulombic efficiency. This is the opposite of what is expected; however, the fit is poor due to many factors affecting a non-linear decay. Additionally, there is extra error due to voltage resolution constraints. Regardless, the trend is negative, as expected due to increased internal cell resistance.

Figure 5.18: The Battery Energy Efficiency for the SPSC LFP battery verse cycle number. Due to the embedded Coulomb counting necessary to derive the energy consumption, a BEE greater than one is found as in the SPSC Coulombic efficiency.

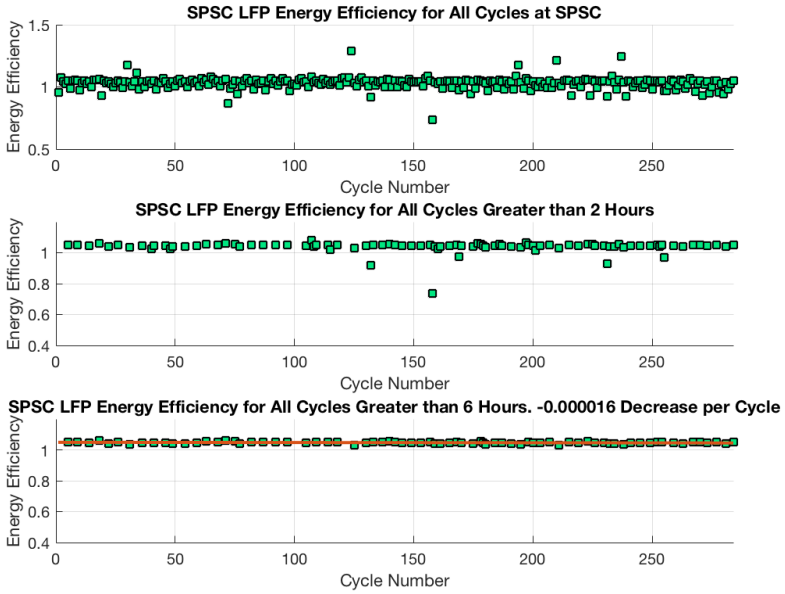

The resultant BEE of the SPSC station is shown in Fig. 5.18. As expected because of the bias error in Coulombic efficiency, this quantity is greater than one. However, there is a net decrease in BEE with more cycles, a trend which is expected, and not entirely disqualified by the bias error.

5.6 Depth of Discharge

As a final metric to identify potential ageing in the LFP battery packs, the Depth of Discharge (DOD) is calculated as unity minus the SOC, and plotted against temperature. While the voltage of an LFP pack during discharge is highly susceptible to the rate of discharge, the LFP packs at the Wilderness Place and SPSC stations experience a very steady discharge rate due to the near constant power consumption of the load. Due to this characteristic, the longer cycles which extend through the night have a very steady and relibably constant discharge. Figure 5.19 shows the distribution of DODs, as well as the voltage vs. DOD curves of the Wilderness Place LFP battery pack.

Figure 5.19: The DOD vs. Cycle Number for the ESS at the Wilderness Place Station is shown on the left. Note: The clear change in DOD around cycle 115, and then again at cycle 170, is the result of the station PV panel being switched from 140W to 100W, and then due to a reduction in load power consumption, respectively. On the right is the voltage vs. DOD for all cycles greater than 5% DOD. A modest variety is present. It must be noted that there is error both dimensions due to the voltage error, and also the current error leading to uncertainty in the actual DOD.

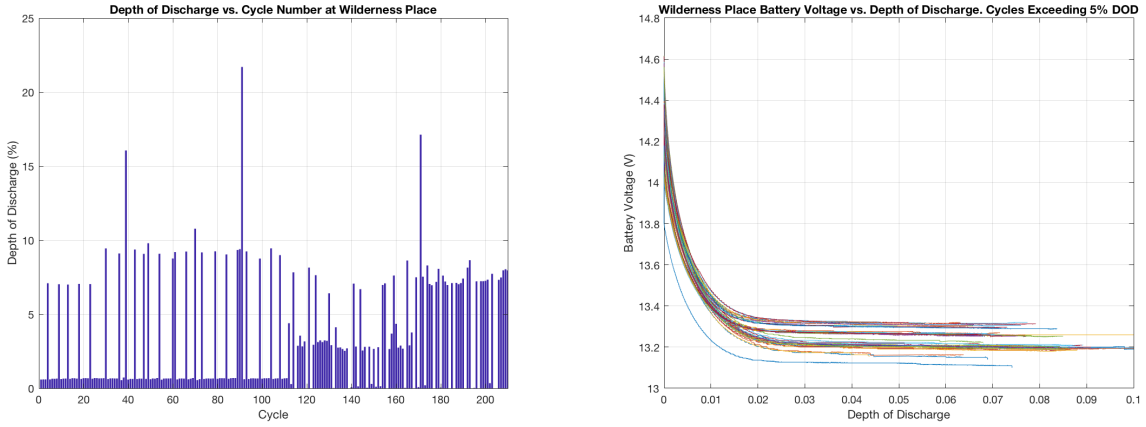

Although the chart of voltage vs. DOD of the Wilderness Place station shows a clear variety in the data, it makes no distinction in the the cycle number. To identify any trends, the voltage at which point the DOD is 5% is taken for each cycle, and then plotted verse cycle number in Fig. 5.20. Of immediate notice is the split in the data set around 110 cycles. This is exactly when the LFP battery was relocated and the Solar PV switched from a 140W to a 100W panel.

As previously discussed, this changed the operation of the system from many intraday cycles and Solar curtailment, to one of balanced Solar/Load power provision and a resultant fewer daily cycles of the LFP resource. When the data is split and the latter half plotted, the right had chart of Fig. 5.20, a slight decrease in voltage is apparent, but non conclusion can be drawn. Note the analog resolution causing the distinct lines of data.

Figure 5.20: The distribution of voltage verse 5% DOD at the Wilderness Place station as a function of cycle number. Two data sets are distinct in the first plot due to the relocation and downsizing of the Solar resource. The chart on the right shows the second half of the data set with respect to cycle length.

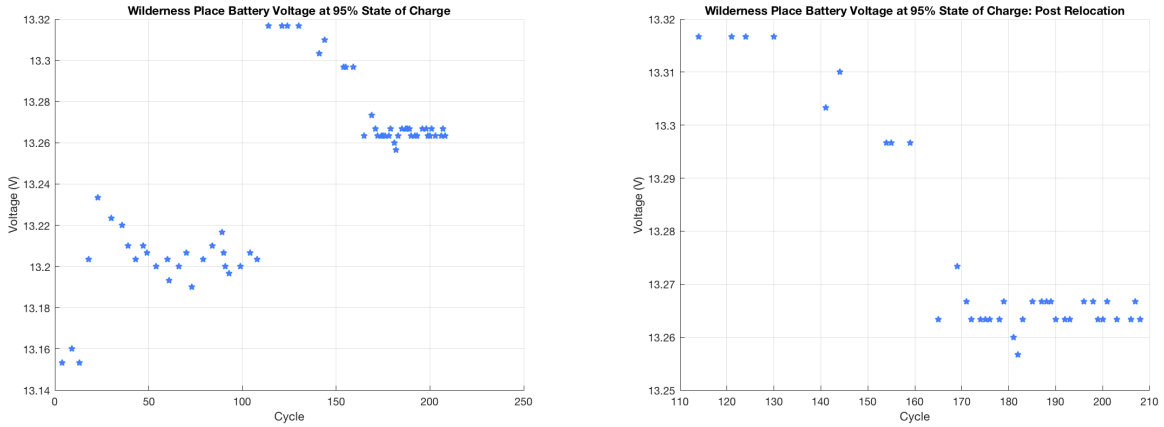

A similar analysis is performed on the Space Sciences station, the results of which are shown in Fig. 5.21. The SPSC shows a far more consistent distributino of DOD, as well as a tighter distribution to a steady voltage vs. DOD curve. The large bias error present in the SPSC data set certainly sheds uncertainty on these plots, but due to its prevalence in the set, the relation of each cycle to each other can be taken as a relative value. The cross section of all voltages at a 5% DOD verse cycle number is shown in Fig. 5.22. There is a decline present with a greater number of cycles, a spread of which is anticipated with age.

Figure 5.21: The DOD distribution and voltage vs. DOD plots of the SPSC station. Although significant error is present in the SPSC data set, it seems to be bias error and thus prevalent in the entire set. As a result, the actual DOD is likely incorrect, but relative to all of the other SPSC battery cycles.

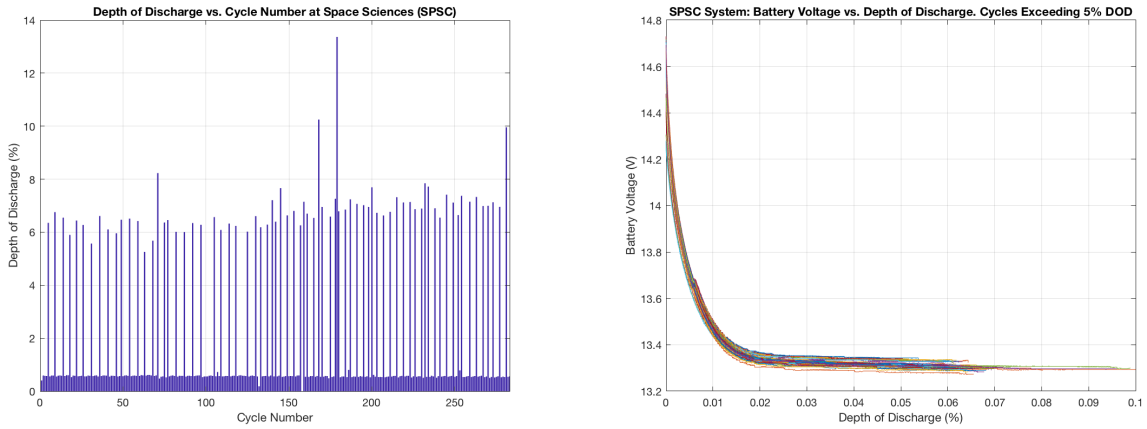

Figure 5.22: The distribution of the voltage vs. 95% SOC of the SPSC battery pack.

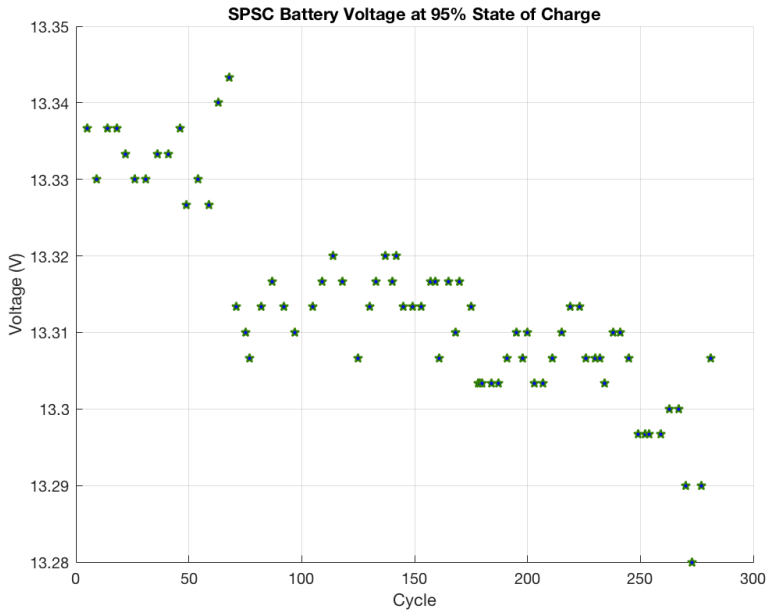

Chapter 6

Conclusion

While providing uninterrupted power to a Wifi Long Distance communications network established on the front range of Colorado, the operation of two LFP Battery Energy Storage Systems was analyzed in an attempt to identify battery deterioriation in isolated microgrids. Using only voltage, current, and temperature monitors at the two stations, large data sets were accrued through the Summer and Fall of 2017 and subsequently analyzed for deterioration indicators. Although the laboratory standard for identifying ageing is to perform a complete charge/discharge cycle of a battery, this is not possible at these remote microgrid stations, and therefore these other metrics are adopted. The primary indicators sought are 'Coulombic Efficiency', the ratio of charge delivered to charge recovered between 100% SOC points, and 'Battery Energy Efficiency', the ratio of energy delivered to energy recovered. As a final metric for ageing, the voltage verse Depth of Discharge curves were analyzed to identify any spread that may indicate ageing.

6.1 Discussion

The data sets were first analyzed to ensure that a continuous set existed with no interruptions which would lead to greater error in subsequent calculations. Schedule Points, locations in the data set at which a 100 % SOC is identified with accuracy by corroborating state changes in the system between the voltage and current measurements, have been found in all continuous Strings of the data. Upon combing the data for all continuous Strings and identifying Schedule Points with an internal algorithm, all sets between Schedule Point are dubbed cycles and all calculations are then

based on a per cycle basis.

Through analysis, it was found that the overall system efficiencies were of acceptable values, but widely varying either due to temperature causing decreases in efficiency, temperature causing measurement error, or a combination of the two. In both the SPSC and Wilderness Place stations, a clear kink in the data is present at 35 degrees C, at which point the precision of the overall efficiencies decays enormously. Regardless, the majority of operation occurs at lower temperatures (sub 35 degrees C), when the system efficiencies were found to be near parity and far more predictable.

6.1.1 Wilderness Place

As the first of two primary metrics for identifiying capacity fade, the Coulombic efficiency is calculated as the summation of all current delivered, and recovered, with respect to time over the charge and discharge intervals within each cycle. For the case of Wilderness Place, a Coulombic efficiency near one (as expected), was identified throughout the lifetime of the battery pack, particularly during the longer cycles. The shorter cycles occur at higher temperatures, which is expected to reduce the Coulombic efficiency due to a greater number of side reactions on account of the Arrhenius relation. When considering only the longer cycles, in which the Coulombic efficiency calculations display more precision, a clear decrease is located with an increasing number of cycles. While this decrease is apparent and expected, there are too many factors involved in altering the individual conditions to make a statement about how this decrease has influeced the State of Health of the Wilderness Place LFP battery.

The Battery Energy Efficiency over the lifetime of the Wilderness Place system also shows a decrease with an increased number of cycles. This was expected on account of the internal resistances of the LFP battery growing with age due to increased diffusion resistance and electrode delamination. Interestingly, although the BEE is expected to be less than the Coulombic efficiency, a slower rate of decay was found. Finally, the voltage verse DOD plots show two partitioned data sets of varying structure, on account of the relocation and downsizing of the Solar PV panel. A slight decline in the discharge voltage at 5% DOD is present in the second half of the data set, but

there is no significance to this aspect.

6.1.2 SPSC

The SPSC system contains more cycles than the Wilderness Place station even though the total operational time is two months less. This is on account of the different operation of the system in which Solar PV is curtailed after a 100% SOC point is reached. The resultant Coulombic efficiencies are found to be greater than one, which is evidence of a gross error as other likely error possibilities, such as the LFP battery decaying as a primary battery source, were ruled out. Regardless, it is shown that even in the presence of a large bias error, a decay in the Coulombic efficiency is still expected. Subsequently one is identifed, albeit at a much lower rate than the Wilderness Place LFP battery. Although the decline in efficiency was identified, again, no conclusion can be made about the impact on SOH, especially considering the error.

As follows from the Coulombic efficiency, the BEE was also found to contain the large bias error, but also display the decline in efficiency of the duration of the experiment. The voltage verse DOD were generated for cycle greater than 5%, and the profile at 5% show a decline in voltage with age. However, the error in Coulomb counting directly effects the DOD estimate which adds substantial error to the voltage measurement due to the non-linearity of the voltage vs. DOD curve, particularly between 0 and 10%. Regardless, it can be said that deterioration is present, but at what quantity, it is not ascertained.

6.2 Closing Remarks

Following the successful deployment of the microgrid systems and connection of the WiLD network, the daily data sets of voltage, current, and temperature measurements were obtainable from each station remotely. With these data sets, operational points of significance (Schedule Points, at 100% SOC) were identified and the cycles bookleafed by these Schedule Points analyzed to derive operational efficiences regarding the operation of the charge controller, and various LFP battery related metrics. Although the presence of too many external influences diminish the abil-

ity to identify a quantity of degradation, deterioration was nonetheless found through decreases in Coulombic, and Battery Energy efficiencies at both the SPSC and Wilderness Place stations. Unfortunately, significant bias error in the SPSC data set resulted in greater than parity efficiences, but a decline still expected even in light of this bias error was located.

The results of this work show promise in developing low tech methods for identifying capacity fade in remote battery stations that prove challenging for traditional capacity fade metrics, those of full charge/discharge cycles and EIS. Although the quantity of degradation was not identifiable, futher work with this dataset, a dataset that will continue to grow over the next years due to the continued operation of the CU Boulder Testbed, may yield trends from which these contributing factors, such as temperature influence, can be isolated and quantified. As a result, this work has created a viable platform upon which more analysis can be protracted from the growing data set to identify ageing and SOH in remote LFP applications.

Bibliography

[1] T. A. Abera, G. Bekele, T. Walter, and P. Adelman. A study of capacity fade and life-cycle estimation of lifepo4 battery based on two years field data. International Journal of Advanced Research in Electrical, Electronics and Instrumentation Engineering, 3:13532–13537, December 2014.

[2] Benedikt Battke, Tobias S. Schmidt, David Grosspietsch, and Volker H. Hoffman. A review and probabilistic model of lifecycle costs of stationary batteries in multiple applications. Elsevier: Renewable and Sustainable Energy Reviews, 25:240–250, 2013.

[3] Marco Bortolini, Mauro Gamberi, and Alessandro Graziani. Technial and economic design of photovoltaic and battery energy storage systems. Elsevier: Energy Conversion and Management, 86:81–92, 2014.

[4] M. J. Bradley and Associates. Powering into the future renewable energy & grid reliability. Report: M.J. Bradley and Associates, 2017.

[5] Anya Castillo and Dennice F. Gayme. Grid-scale energy storage applications in renewable energy integration: A survey. Elsevier: Energy Conversion and Management, 87:885–894, 2014.

[6] California Independent System Operator Corporation. Moorpark sub-area local capacity alternative study. 2017.

[7] Paul Denholm, Josh Eichman, and Robert Margolis. Evaluating the technical and economic performance of pv plus storage power plants. Report: National Renewable Energy Laboratory, 2017.

[8] Will Driscoll. Growth prospects for the global grid-connected battery market. Green Tech Media, 2017. August 16, 2017.

[9] Bruce Dunn, Haresh Kamath, and Jean-Marie Tarascon. Electrical energy storage for the grid: A battery of choices. Science Magazine, 334, 2011.

[10] David Feldman, Robert Margolis, Paul Denholm, and Joseph Stekli. Exploring the potential competitiveness of utility-scale photovoltaics plus batteries with concentrating solar power, 20152030. Report: National Renewable Energy Laboratory, 2016.

[11] Garrett Fitzgerald, James Mandel, Jesse Morris, and Herve Touati. The economics of battery energy storage. Rocky Mountain Institute Report, 2015.

[12] Franhaufer-Institute for Solar Energy Systems. Current and future costs of photovoltaics, 2015.

[13] S. Franger, C. Bourbon, and F. Le Cras. Optimized lithium iron phosphate for high-rate electrochemical applications. Journal of The Electrochemical Society, 151:1024–1027, 2004.

[14] Ran Fu, David Feldman, Robert Margolis, Mike Woodhouse, and Kristen Ardani. U.s. solar photovoltaic system cost benchmark: Q1 2017. National Renewable Energy Laboratory: Report, 2017.

[15] M. Garcia-Plaza, J. Eloy-Garcia Carrasco, A Pena-Asensio, J. Alonso-Martinez, and S. Arnaltes Gomez. Hysteresis effect influence on electrochemical battery modeling. Elsevier: Electric Power Systems Research, 152:27–35, 2017.

[16] Sebastien Grolleau, Arnaud Delaille, Hamid Gualous, Philippe Gyan, Renaud Revel, Julien Bernard, Eduardo Redondo-Iglesias, and Jeremy Peter. Calendar aging of commercial graphite/lifepo4 cell predicting capacity fade under time dependent storage conditions. Elsevier: Journal of Power Sciences, 255:450–458, February 2013.

[17] The Brattle Group. Comprehensively valuing battery storage in california. 2017.

[18] Clemens Guenther, Benjamin Schott, Wilfried Hennings, Paul Waldowski, and Micheal A. Danzer. Model-based investigation of electric vehicle battery aging by means of vehicle-to-grid scenario simulations. Elsevier: Journal of Power Sources, 239:604–610.

[19] Yao He, XingTao Liu, ChenBin Zhang, and ZongHai Chen. A new model for state-of-charge (soc) estimation for high-power li-ion batteries. Elsevier: Applied Energy, 101:808–814, 2012.

[20] Paul Hibbard, Susan Tierney, and Katherine Franklin. Electricity markets, reliability and the evolving u.s. power system. Report from the Analysis Group: Economic, Financial, and Strategy Consultants, 2017.

[21] Anderson Hoke, Alexander Brissette, Dragan Maksimovic, Annabelle Pratt, and Kandler Smith. Electric vehicle charge optimization including effects of lithium-ion battery degradation. IEEE Xplore, 2011.

[22] Xiaosong Hu, Shengbo Li, and Huei Peng. A comparative study of equivalent circuit models for li-ion batteries. Elsevier: Journal of Power Sources, 198:359–367, 2012.

[23] Xiaosong Hu, Shengbo Li, Huei Peng, and Fengchun Sun. Charging time and loss optimization for linmc and lifepo4 batteries based on equivalent circuit models. Elsevier: Journal of Power Sources, 239:449–457, April 2013.

[24] Verena Julch. Comparison of electricity storage options using levelized cost of storage (lcos) method. Elsevier: Applied Energy, 183:1594–1606, 2016.

[25] Stefan Kabitz, Jochen Bernhard Gerschler, Madeleine Ecker, Yusuf Yurdagel, Brita Emmermacher, Dave Andre, Tim Mitsch, and Dirk Uwe Sauer. Cycle and calendar life study of a graphitejlini1/3mn1/3co1/3o2 li-ion high energy system. part a: Full cell characterization. Elsevier: Journal of Power Sources, 239:572–583, March 2013.

[26] M. Kassem, J. Bernard, R. Revel, S. Pelissier, F. Duclaud, and C. Delacourt. Calendar aging of a graphite/lifepo4 cell. Elsevier: Journal of Power Sources, 208:296–305, February 2012.

[27] Rick Wallace Kenyon and Alan Mickelson. A testbed for wildnet and white space. IEEE 2016 Global Humanitarian Technology Conference, pages 143–150, 2016.

[28] Michael Koller, Theodor Borsche, Andreas Ulbig, and Goran Andersson. Review of grid applications with the zurich 1 mw battery energy storage system. Elsevier: Electric Power Systems Research, 120:128–135, 2015.

[29] Matthew T. Lawder, Bharatkumar Suthar, Paul W. C. Northrop, Sumitava De, C. Michael Hoff, Olivia Leitermann, Mariesa L. Crow, Shriramm Santhanangopalan, and Venkat R. Subramanian. Battery energy storage system (bess) and battery management system (bms) for grid-scale applications. Proceedings of the IEEE, 102, 2014.

[30] Yuhan Liang, Jing Su, Beidou Xi, Yajuan Yu, Danfeng Ji, Yuanyuan Sun, Chifei Cui, and Jianchao Zhu. Life cycle assessment of lithium-ion batteries for greenhouse gas emissions. Elsevier: Resources, Conservation and Recycling, 117:285–293, November 2016.

[31] Languang Lu, Xuebing Han, Jianqiu Li, Jianfeng Hua, and Minggao Ouyang. A review on the key issues for lithium-ion battery management in electric vehicles. Elsevier: Journal of Power Sciences, 226:272–288, 2014.

[32] Xing Luo, Jihong Wang, Mark Dooner, and Jonathan Clarke. Overview of current development in electrical energy storage technologies and the application potential in power system operation. Elsevier: Applied Energy, 137:511–536, 2014.

[33] Abhishek Malhotra, Benedikt Battke, Martin Beuse, Annegret Stephan, and Tobias Schmidt. Use cases for stationary battery technologies: A review of the literature and existing projects. Elsevier: Renewable and Sustainable Energy Reviews, 56:705–721, 2015.

[34] Peter Maloney. An inside look at using energy storage to integrate renewable resources. Utility Dive, 2017.

[35] M. Mastali, J. Vazquez-Arenas, R. Fraser, M. Fowler, S. Afshar, and M. Stevens. Battery state of charge estimation using kalman filtering. Elsevier: Journal of Power Sources, 239:294–307, 2013.

[36] Joyce McLaren, Pieter Gagnon, Kate Anderson, Emma Elgqvist, Ran Fu, and Tim Remo. Battery energy storage market: Commercial scale, lithium-ion project in the u.s. Slide Deck: National Renewable Energy Laboratory, 2016.

[37] Alan Mickelson, Rick Wallace Kenyon, Heinz Ulrich Boehmer Fiehn, and Mark Hinkle. Management of distributed electrical storage in wide area communications systems. IEEE SmartCity 2017, 2017.

[38] Alan Mickelson, Rick Wallace Kenyon, Bennett Miller, Mark Hinkle, Stefano Costa, Nicholas Bollen, Chris Dizon, Heinz Ulrich Boehmer FIehn, and Kailin Yahime Mazotti. University of colorado at boulder wildnet testbed. IEEE 2017 Global Humanitarian Technology Conference, 2017.

[39] Maik Naumann, Andreas Jossen, Cong Nam Truong, and Holger Hesse. Lithium-ion battery cost analysis in pv - household application. Elsevier: Energy Procedia, 73:37–47, 2015.

[40] Adnan Nuhic, Tarik Terzimehic, Thomas Soczka-Guth, Michael Buckholz, and Klaus Dietmayer. Health diagnosis and remaining useful life prognostics of lithium-ion batteries using data-driven methods. 239:680–688, 2012.

[41] Noshin Omar, Mohamed Abdel Monem, Yousef Firouz, Justin Salminen, Jelle Smekans, Omar Hegazy, Hamid Galous, Grietus Mulder, Peter Van den Bossche, Thierry Coosemans, and Joeri Van Mierlo. Lithium iron phosphate based battery assessment of the aging parameters and development of cycle life model. Elsevier: Applied Energy, 113:1575–1585, 2014.

[42] A. Opitz, P. Badami, L. Shen, K. Vignarooban, and A.M. Kannan. Can li-ion batteries be the panacea for automotive applications? Elsevier: Renewable and Sustainable Energy Reviews, 68:685–692, October 2016.

[43] Sebastian Paul, Christian Diegelmann, Herbert Kabza, and Werner Tillmetz. Analysis of ageing inhomogeneities in lithium-ion battery systems. Elsevier: Journal of Power Sources, 239:642–650, January 2013.

[44] Ilja Pawel. The cost of storage - how to calculate the levelized cost of stored energy (lcoe) and applications to renewable energy generation. Elsevier: Energy Procedia, 46:68 – 77, 2014.

[45] Guido Plessmann, Matthias Erdmann, Markus Hlusiak, and Christian Breyer. Global energy storage demand for a 100% renewable electricity supply. Elsevier: Energy Procedia, 46:22–31, 2014.

[46] Andreas Poullikkas. A comparative overview of large-scale battery systems for electricity storage. Elsevier: Renewable and Sustainable Energy Reviews, 27:778–788, 2013.

[47] M. Reichert, D. Andre, A. Rosmann, P. Janssen, H-G. Bremes, D. U. Sauer, S. Passerini, and M. Winter. Influence of relaxation time on the lifetime of commercial lithium-ion cells. Elsevier: Journal of Power Sources, 239:45–53, March 2013.

[48] Jurgen Remmlinger, Michael Buchholz, Thomas Soczka-Guth, and Klaus Dietmayer. On-board state-of-health monitoring of lithium-ion batteries using linear parameter-varying models. Elsevier: Journal of Power Sources, 239:689–695, November 2012.

[49] M. Safari and C. Delacourt. Aging of a commerical graphite/lifepo4 cell. Journal of Electrochemical Society, 158:1123–1135, 2011.

[50] Mushifiqur R. Sarker, Matthew D. Murbach, Daniel T. Schwartz, and Miguel A. Ortega-Vazquez. Optimal operation of a battery energy storage system: Trade-off between grid economics and storage health. Elsevier: Electric Power Systems Research, 152:342–349, 2017.

[51] R P Sasmal, Subir Sen, and Ankur Chakraborty. Solar photovotaic output smoothing: Using battery energy storage system. National Power Systems Conference, 2016.

[52] Eugene Shlatz, Dave Larsen, Steven Tobias, and Michael De Paolis. San joaquin valley distributed energy resource. Navigant Report prepared for California Energy Commision, 2016.

[53] Xin Sun, Han Hao, Fuquan Zhao, and Zongwei Liu. Tracing global lithium flow: A trade-linked material flow analysis. Elsevier: Resources, Conservation, and Recycling, 124:50–61, 2017.

[54] John R. Taylor. An Introduction to Error Analysis.

[55] Olivier Tremblay, Louis-A. Dessaint, and Abdel-Illah Dekkiche. A generic battery model for the dynamic simulation of hybrid electric vehicles. IEEE Xplore, pages 283 – 289, 2007.

[56] Laurent Vandepaer, Julie Cloutier, and Ben Amor. Environmental impacts of lithium metal polymer and lithium-ion stationary batteries. Renewable and Sustainable Energy Reviews, 78:46–60, April 2017.

[57] J. Vetter, P. Novak, M. R. Wagner, C. Veit, K. C. Moller, J. O. Besenhard, M. Winter, M. Wohlfahrt-Mehrens, C. Vogler, and A. Hammouche. Ageing mechanisms in lithium-ion batteres. Elsevier: Journal of Power Sources, 147:269–281, 2005.

[58] Matthew L. Wald. Hold that megawatt! New York Times: Green Blog, 2011. Available at `https://green.blogs.nytimes.com/2011/01/07/hold-that-megawatt/?mcubz=0`.

[59] Xingchi Wang, Peter Adelmann, and Thomas Reindl. Use of lifepo4 batteries in stand-alone solar system. Elsevier: Energy Procedia, 25:135–140, 2011.

[60] M. Stanley Whittingham. History, evolution, and future status of energy storage. Proceedings of the IEEE, 100, 2012.

[61] Yong Zheng, Yan-Bing He, Kun Qian, Baohua Li, Xindong Wang, Jianling Li, Sum Wai Chiang, Cui Miao, Feiyu Kang, and Jianbo Zhang. Deterioration of lithium iron phosphate/graphite power batteries under high-rate discharge cycling. Elsevier: Electrochimica Acta, 176:270–279, 2015.

[62] Liang Zhong, Chenbin Zhang, Yao He, and Zonghai Chen. A method for the estimation of the battery pack state of charge based on in-pack cells uniformity analysis. Elsevier: Applied Energy, 113:558–564, 2014.

[63] A.I. Zia and S.C. Mukhopadhyay. Electrochemical Sensing: Carcinogens in Beverages.

Appendix A

Supporting Documents/Images

Supporting documents and images for the project.

Figure A.1: The voltage and current flow at the Wilderness Place station, June 6 - 30, 2017

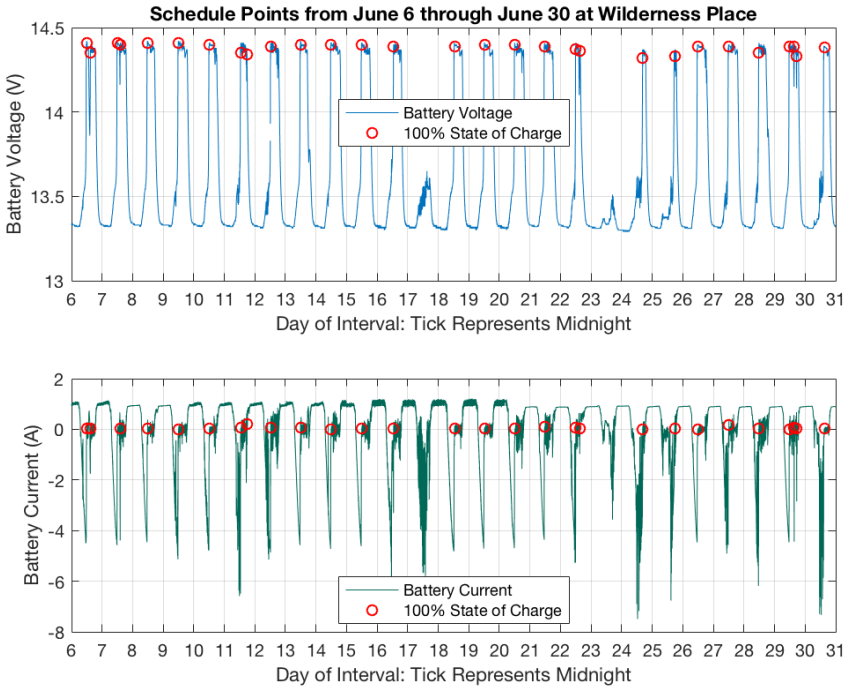

Figure A.2: As an example, the following shows the battery current data from June 6 both before and after the calibration has been applied. While the offset is most prevalent during periods of consistent current flow, the scaling factor influence becomes obvious at points of high current flow (see 40,000 seconds).